

INDIAN INSTITUTE OF TECHNOLOGY, BOMBAY

DEPARTMENT OF PHYSICS



BACHELOR'S THESIS (2024-25)

Topological Figure of Merit Optimization for Valley Photonic Crystals

Devansh Satra

210110037

Supervisors

Professor Anshuman Kumar, LOQM, IIT Bombay

Professor Abhishek Kumar, UTSP Lab, JNCASR

Abstract

The exponential growth in global data demands, driven by the ever-increasing number of interconnected devices and immersive applications such as augmented reality, holographic communication, and the Internet of Things (IoT), necessitates the development of advanced wireless networks capable of terabit-per-second data rates with sub-millisecond latency. Terahertz (THz) frequencies, spanning from 0.1 to 10 THz, present a compelling solution for sixth-generation (6G) wireless communication due to their vast spectral bandwidth, enabling significantly higher data throughput. However, several critical challenges—including severe path loss, atmospheric attenuation, and limitations of current THz source technologies—must be addressed to harness the full potential of this spectral region.

To overcome these challenges, we leverage topological photonic crystals (TPCs), particularly Valley Photonic Crystals (VPCs), which exhibit topological protection through robust edge states. These valley-polarized modes, characterized by unique Berry curvature distributions and valley-dependent Chern numbers, enable defect-tolerant waveguiding through complex geometries, making VPCs exceptionally suitable for scalable, high-efficiency THz communication systems.

In this work, we develop a comprehensive computational framework to analyze and optimize topological photonic structures tailored for 6G communication devices. Using the Plane Wave Expansion (PWE) method, our simulations rigorously calculate photonic band structures, Berry curvature, and Chern numbers for diverse VPC configurations, providing new insights into the relationships between geometry and topological properties. To systematically explore previously uncharted geometries, we employ Bayesian optimization to maximize a figure-of-merit, revealing specific designs that achieve unprecedented robustness and enhanced performance in the THz range.

Our results demonstrate that strategic geometric modifications of VPCs lead to significant improvements in topological robustness, and defect tolerance, thus providing a viable pathway towards reliable THz integrated circuits for 6G networks. This research lays a foundational framework for the design of next-generation THz communication devices, addressing current technical limitations and paving the way for ultra-reliable, high-speed wireless networks.

Contents

Abstract	1
1 Introduction	7
2 Valley Photonic Crystals	12
2.1 Fundamentals of Valley Degrees of Freedom	12
2.2 Valley-Contrasting Physics and Orbital Magnetic Moments	13
2.3 Analogies to Other Topological Systems	15
2.4 Mathematical Formulation of Valley Polarization	16
2.5 Topological Protection in Valley Photonic Crystals	16
2.6 Practical Example: Waveguiding Applications of VPCs	17
2.7 Berry Curvature and Chern Numbers in VPCs	18
3 Methodology	19
3.1 Mathematical Derivation of PWE Method for Photonic Crystals	21
3.1.1 Eigen-equations from Maxwell's Equations	21
3.1.2 Eigen-equation in TE (Transverse Electric) Mode	22
3.1.3 Inverse Dielectric Function and Field Eigenstates	23
3.1.4 Master Equation, Eigenmatrix Construction in 2D PhCs	24
3.1.5 Fourier Coefficients	26
3.2 Computation of Topological Properties	27
3.3 Computation of Electric and Magnetic Fields	28
3.4 Poynting Vector and Power Flow	29
3.5 Convergence Testing	29
3.5.1 Convergence with Number of Plane Waves	30
3.5.2 Convergence of Chern Number with Integration Area	33
3.5.3 Convergence with Discretization of the Brillouin Zone	34
3.5.4 Summary of Convergence Testing	35

4 Optimization Results and Methodology	36
4.1 Introduction to Bayesian Optimization	36
4.1.1 Why Bayesian Optimization?	37
4.2 Time Complexity Analysis	38
4.3 Figure of Merit	38
4.4 Bayesian Optimization Implementation Details	38
4.4.1 Design Parameters and Ranges	39
4.4.2 Optimization Process	39
4.5 Results and Analysis	40
4.5.1 Optimization Results	40
4.5.2 Parameter Analysis and Convergence Study	41
5 Future Work and Conclusion	43
5.1 Exploring Alternative Optimization Techniques	43
5.1.1 Gradient-free Methods: Particle Swarm Optimization	43
5.1.2 Adjoint Method-Based Shape Optimization	44
5.1.3 Moving Towards Neural Network-Based Optimization	44
5.2 Detailed Study on Fabrication Imperfections	44
5.3 Ongoing Study on Dirac Frequency	46
5.4 Pathway to Experimental Validation	46
5.5 Conclusion	47
6 Modified PSO Optimization Methodology	49
6.1 Mixed-Integer Particle Swarm Optimization Algorithm	51
6.1.1 Design Variables and Parameterization	51
6.1.2 Swarm Initialization and Update Equations	52
6.1.3 PSO Parameter Update Strategies	53
6.2 Topological Objective Function and Evaluation Pipeline	57
6.3 Optimization Results and Discussion	59
6.3.1 Visualization and Analysis of Optimization Landscape	59
7 COMSOL Waveguiding Simulations	65
7.1 Waveguide Model Setup in COMSOL	66
7.2 Simulation Results and Discussion	70

8 Future Work and Conclusion	75
8.1 Future Work	75
8.2 Conclusion	75

BTP 1 - Autumn Semester (2024–25)

Chapters 1 to 5 of this thesis were completed in the Autumn Semester (2024-25) as part of the work done in PH 587 - B.Tech. Project 1.

This includes the theoretical foundations, PWE methodology, numerical convergence analysis, and Bayesian optimization of Valley Photonic Crystals.

Chapter 1

Introduction

The field of photonics has made significant strides in recent years, primarily by harnessing the ability of materials to manipulate light through engineered structural properties. Photonic crystals (PhCs), characterized by their periodic dielectric modulation, offer unparalleled control over light propagation. This is achieved by creating photonic band gaps that can selectively inhibit or transmit specific frequencies, with robust properties often arising from their underlying topology. These capabilities have driven innovations in light control, finding applications in technologies such as low-threshold lasers, optical communications, and integrated photonic circuits.

Photonics is a natural candidate for solving many of the challenges faced by sixth-generation (6G) communications due to its inherent wavelength-dependent scalability, compatibility with CMOS technology, and ability to offer precise control over light propagation. The integration of photonic solutions into existing technologies promises both increased performance and improved energy efficiency, key requirements for 6G.

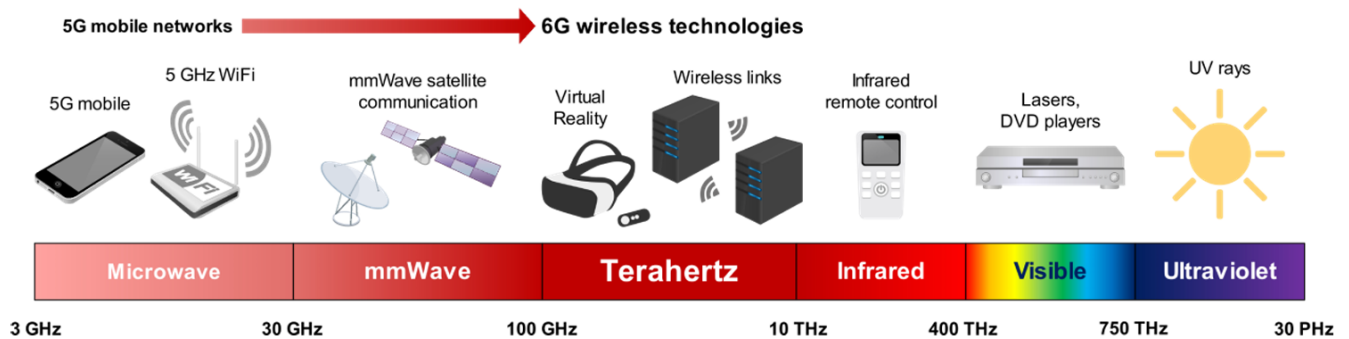


Figure 1.1: The THz band in the electromagnetic spectrum for 6G technologies.[1]

The exponential growth in data-driven applications, including immersive technologies such as augmented and virtual reality (AR/VR), holographic communication, and the expanding Internet of Things (IoT), has placed enormous pressure on current wireless networks. This surge in demand necessitates a transition toward the sixth generation (6G) of wireless technology, which seeks to deliver terabit-per-second data rates with sub-millisecond latency. Such requirements are beyond the capabilities of existing millimeter-wave networks, thus prompting the exploration of the terahertz (THz) frequency band as a crucial enabler for 6G. THz frequencies (0.1–10 THz) provide an order-of-magnitude increase in available bandwidth, allowing for substantially higher data throughput, as suggested by the Shannon-Hartley theorem, which states that increasing the available bandwidth results in a linear increase in channel capacity—a crucial factor for achieving high data-rate communication. The theorem states that the upper bound of channel capacity C (or the maximum theoretical data rate) is given by:

$$C = W \log_2 \left(1 + \frac{P}{N} \right)$$

where P is the average transmitted power, N is the average power of white noise over the bandwidth W , with $\frac{P}{N}$ being the signal-to-noise ratio.

Adopting THz frequencies is pivotal for achieving the extreme data rates and low latency demanded by 6G applications. Occupying the spectral region between microwaves and infrared light, THz waves have historically been underutilized due to challenges in generation, guiding, and detection. Atmospheric attenuation, particularly from water vapor, imposes significant limitations on propagation range, while compact and powerful THz sources remain limited. Despite these difficulties, THz frequencies offer unique advantages for communication, including narrow beamwidths and highly directional propagation, which enhance communication security by reducing signal interception and improving beam-steering capabilities. Furthermore, the shorter wavelength of THz radiation enables component miniaturization, making it feasible to integrate THz devices into compact, high-density environments, such as data centers and on-chip systems. However, innovative solutions are needed to overcome inherent challenges such as high path loss, limited transmission range, and device sensitivity to imperfections.

To address the limitations of conventional THz waveguides, topological photonic crystals (TPCs) offer a promising alternative by utilizing principles from topological

physics to achieve robust, defect-tolerant waveguiding. Conventional THz waveguides, such as metallic hollow waveguides and dielectric structures, often suffer from significant bending losses, ohmic losses, and a high sensitivity to fabrication imperfections. These limitations hinder their effectiveness for practical use in complex communication systems. Photonic topological insulators (PTIs), inspired by condensed matter physics, provide a solution by supporting protected edge states that are resilient to backscattering and imperfections—qualities essential for reliable THz communication. A specific class of PTIs, Valley Photonic Crystals (VPCs), is particularly well-suited for THz applications because they exploit the valley degree of freedom to support unidirectional, topologically protected edge states.

Valley Photonic Crystals possess unique physical properties that make them suitable for THz communication:

- Robustness Against Disorder and Imperfections: The topological edge states in VPCs are immune to scattering from sharp bends and structural imperfections, enabling reliable THz wave transmission even in complex geometries.
- High Bandwidth Efficiency: VPCs provide single-mode, linear-dispersion edge states, which minimize signal delay across different frequencies and enhance bandwidth utilization.
- Silicon Platform Compatibility: VPCs can be fabricated on silicon substrates, which align with complementary metal-oxide-semiconductor (CMOS) technology, facilitating large-scale integration and cost-effective deployment of THz devices for high-density applications.

Recent advancements in VPCs for THz applications underscore their potential to transform communication systems. Previous THz technologies faced significant obstacles, including high losses through bends and fabrication difficulties. However, VPCs, with their topologically protected edge states, address these issues effectively. Experimental studies by Yang, Y., Yamagami, Y., Yu, X. et al. [2] have demonstrated that valley-polarized kink states retain over 99 % transmission efficiency even in the presence of structural defects, showcasing their robustness in realistic settings, far surpassing the limitations of conventional THz waveguides. These robust properties stem from unique topological features, including Berry curvature and valley Chern numbers, which are engineered by breaking inversion symmetry in photonic crystal lattices.

The robustness and versatility of VPCs make them ideal for high-speed, on-chip THz interconnects in 6G infrastructure, supporting next-generation applications such as real-time healthcare data streaming, autonomous vehicle networks, and high-definition video transmission. Nevertheless, further exploration is necessary to fully characterize optimal VPC configurations, including trade-offs between design complexity, fabrication tolerance, and overall performance.

Objectives

This study aims to advance the design and computational optimization of topological photonic structures for THz communication by developing a comprehensive framework that enables detailed analysis and enhancement of VPC geometries. Using the Plane Wave Expansion (PWE) method, this research will:

Calculate the photonic band structure, Berry curvature, and Chern numbers for various VPC configurations.

Systematically optimize design parameters using Bayesian optimization to maximize robustness and minimize losses, with a particular focus on reducing bending loss and enhancing spectral efficiency.

Explore untested VPC geometries to identify configurations that exhibit high defect tolerance, spectral efficiency, and resilience against fabrication imperfections.

Our approach provides a systematic pathway to assess and refine the performance of VPCs under realistic conditions, setting the stage for experimental validation and practical application in THz integrated circuits. This research thus contributes foundational insights for the design of robust THz waveguides, with the potential to revolutionize on-chip and short-range wireless communication in 6G networks.

Future Directions and Potential Applications

The findings of this study underscore the potential of VPCs in enabling robust, high-capacity THz communication. Looking ahead, several avenues for future exploration include:

- Advanced Optimization Techniques: Incorporating gradient-free and adjoint-based methods, or leveraging machine learning algorithms, could further refine VPC designs and facilitate their application across a wider range of devices.

- Experimental Fabrication and Testing: The insights from this work will guide the experimental realization of VPC-based devices, allowing for performance validation and real-world assessment in 6G communication settings.
- Applications in Integrated Photonics and Beyond: Beyond wireless communication, VPCs hold promise for various photonic applications, such as THz sensors, high-density data interconnects, and advanced optical devices.

Conclusion

This study addresses critical challenges in THz communication by advancing the design and optimization of topologically protected VPCs for next-generation applications. The findings establish a roadmap for future experimental work, marking a significant step toward integrating VPC-based THz devices into practical 6G systems, with far-reaching implications for ultra-reliable, high-speed wireless networks and photonic integrated circuits.

Topological photonic crystals (TPCs), a subset of PhCs, exploit mathematical invariants—such as Berry curvature and Chern numbers—to protect specific light modes. These invariants enable novel light manipulation strategies, including unidirectional waveguiding that is immune to backscattering, even in the presence of defects. By designing custom simulations based on the PWE method, this study extends the computational modeling of TPCs to novel, previously unexplored geometries. The objective is to determine the influence of geometric variations on critical topological properties and identify designs that can enhance the performance of photonic devices.

In this report, we present a detailed computational approach that models the photonic band structure, Berry curvature, and Chern number of various TPC geometries. We assess each configuration's potential for robust, topologically protected states, which are essential for developing resilient optical communication channels and photonic circuits. By bridging computational techniques and photonic material design, this research aims to expand the current knowledge on TPCs, contributing to the development of next-generation photonic devices.

Chapter 2

Valley Photonic Crystals

Valley Photonic Crystals (VPCs) represent an advanced mechanism for achieving robust, defect-resistant wave propagation in photonic devices, leveraging the unique physical properties of valley degrees of freedom (DOF). In this section, we provide an in-depth exploration of the underlying physics of VPCs, focusing on the concepts of valley degrees of freedom in momentum space, valley polarization, and topological protection. We elaborate on the theoretical foundations, mathematical formulations, and practical examples to demonstrate how VPCs enable applications in waveguiding, terahertz (THz) communication, and integrated photonic circuitry.

2.1 Fundamentals of Valley Degrees of Freedom

In condensed matter physics, valleys correspond to the local extrema in the electronic band structure that appear at specific high-symmetry points within the Brillouin zone, such as the K and K' points in a hexagonal lattice. These valleys, much like electron spin in spintronics, serve as an additional degree of freedom—referred to as the valley pseudospin—that can be exploited for information storage and processing. The concept of utilizing valley DOFs, termed valleytronics [3][4], was first demonstrated in two-dimensional materials like MoS₂, illustrating the potential of valleys as carriers of information.

The analogy between valley DOFs and electron spin can be understood in the context of **spintronics**, where electron spin is manipulated to encode and process information. Similarly, **valleytronics** exploits the existence of distinct valleys in the band structure as an additional pseudospin. This analogy emphasizes why valley degrees of freedom are powerful in the context of electronic and optical systems: they can be

selectively manipulated using external fields, such as electric or magnetic fields, or by breaking specific symmetries in the underlying lattice. Historically, the realization of valleytronics began with the pioneering work on detecting topological valley currents in graphene superlattices [5], on the valley-Hall effect in MoS₂ in 2014 [6] and the demonstration of topological valley transport in bilayer graphene in 2015 [7]. These milestones provided foundational evidence for how valley physics could be harnessed in practical applications and laid the groundwork for extending these concepts to optical systems, such as photonic crystals.

In the context of photonic crystals, valleys emerge in the photonic band structure of two-dimensional honeycomb lattices. Crucially, breaking inversion symmetry (\mathcal{I}) at the lattice level allows one to distinguish between the K and K' valleys, resulting in valley-contrasting physics. This symmetry breaking leads to local Berry curvatures with opposite signs at the K and K' valleys, lifting the degeneracy at the Dirac points and resulting in the formation of massive Dirac cones. Consequently, valley polarization arises, wherein each valley supports distinct optical modes with opposite circular polarizations. This additional degree of freedom—valley pseudospin—serves a similar function to electron spin and can be harnessed for encoding information.

2.2 Valley-Contrasting Physics and Orbital Magnetic Moments

The concept of **valley-contrasting physics** is fundamental to the operation of VPCs. The valleys at K and K' points in the band structure exhibit contrasting behaviors due to the self-rotation of the Bloch states near these points. This self-rotation induces **valley-dependent orbital magnetic moments**, which arise from the different angular momentum characteristics of the Bloch states at each valley. In essence, the opposite rotations at valleys K and K' result in opposite orbital magnetic moments, leading to **valley-locked** orbital magnetism. This property is crucial for realizing robust photonic topological states, as it enables the valleys to behave like effective magnetic dipoles that interact differently with external perturbations, thus providing a mechanism to protect valley-polarized states from scattering.

When inversion symmetry (\mathcal{I}) is broken in a two-dimensional honeycomb lattice, such as in photonic crystals, a mass term is introduced in the effective Hamiltonian near the Dirac points. This mass term causes a splitting of the Dirac cones, resulting

in valley-contrasting Berry curvature. The Berry curvature ($\Omega(k)$) acts as an effective magnetic field in momentum space, with opposite signs at the K and K' valleys. This non-zero Berry curvature is a direct consequence of broken inversion symmetry and is responsible for many of the topological properties exhibited by VPCs. It allows the valleys to support **topologically protected edge states** that are immune to certain types of scattering, as long as inter-valley scattering is suppressed. The presence of valley-locked orbital magnetic moments, coupled with valley-contrasting Berry curvature, ensures that photons remain confined to specific pathways, even in the presence of structural imperfections [?].

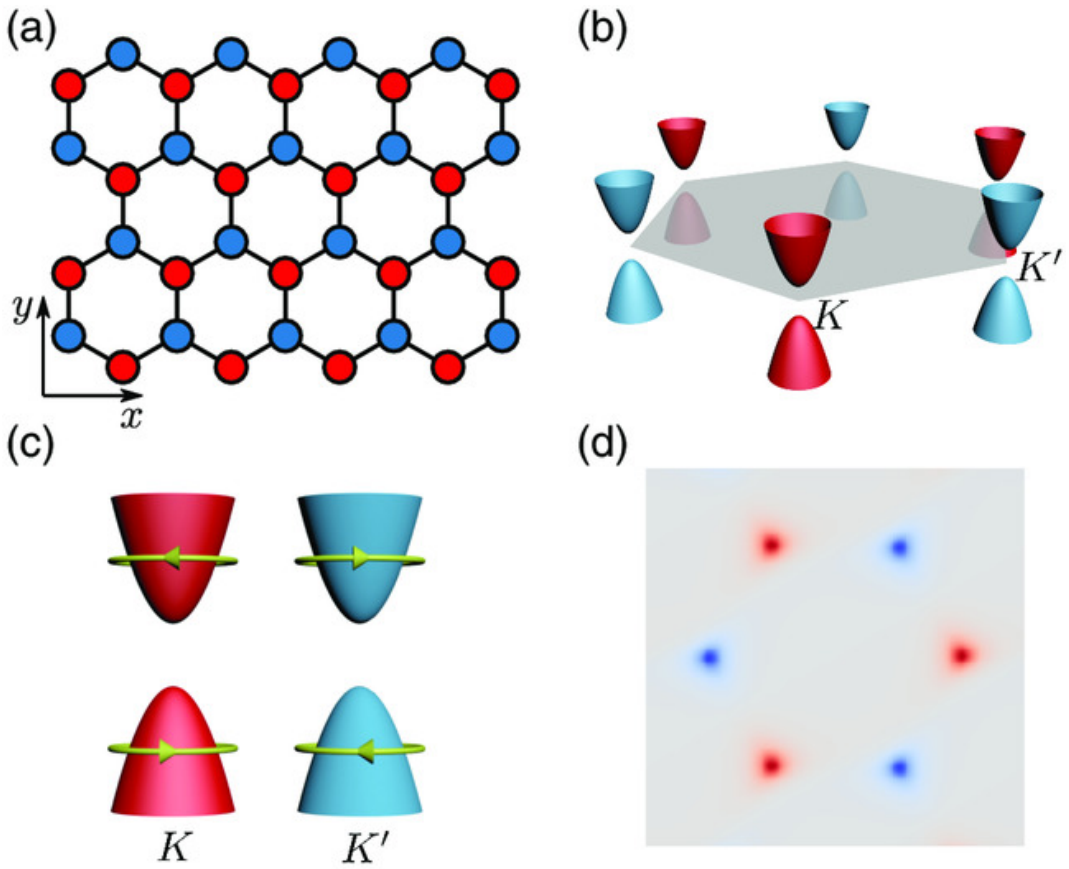


Figure 2.1: **Valley-contrasting Physics** [8] (a) A honeycomb lattice with nearest-neighbor coupling, where red and blue sites have on-site energies M and $-M$, respectively. (b) Massive Dirac cones located at the corners of the Brillouin zone. The gray hexagon denotes the Brillouin zone, with red (blue) indicating Dirac cones at the K (K') valleys. (c) Bloch states at opposite valleys exhibit opposite self-rotation, resulting in valley-locked orbital magnetic moments. (d) Berry curvature distribution: gray represents zero curvature, while red (blue) shows positive (negative) nonzero values. Berry curvature is concentrated at the valleys, with opposite signs at each valley.

In a two-dimensional honeycomb lattice, the inversion symmetry (\mathcal{I}) breaking is a crucial factor that distinguishes the K and K' valleys. The absence of \mathcal{I} in the lattice enables the formation of massive Dirac cones at the K and K' points, introducing valley-contrasting properties that can be harnessed for information processing. These valley-polarized modes are essential in designing devices that utilize valley degrees of freedom for reliable data transmission (see Figure 2.1).

2.3 Analogies to Other Topological Systems

VPCs share similarities with other well-known topological phases, such as the quantum Hall and quantum spin Hall effects, but differ fundamentally in terms of symmetry and topological invariants. For example, the quantum Hall phase arises from **breaking time-reversal symmetry** via an external magnetic field, leading to **chiral edge states characterized by an integer Chern number**. On the other hand, the quantum spin Hall phase **preserves time-reversal symmetry and features helical edge states**, which are protected by **spin-Chern numbers**.

In contrast, the valley-Hall phase observed in VPCs is driven by **breaking inversion symmetry** while preserving time-reversal symmetry. This phase is characterized by the **half-integer valley-Chern number**, which leads to **valley-polarized edge states**. The unique feature of VPCs is their **reliance on intrinsic lattice symmetries** and geometric properties **rather than external magnetic fields**, making them more versatile for photonic applications.

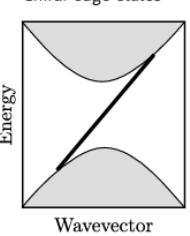
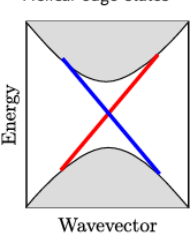
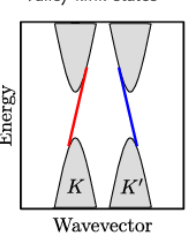
	Quantum Hall phase	QSH phase	Valley-Hall phase
Topological invariant	Chern number	\mathbb{Z}_2 index/spin-Chern number	Valley-Chern number
Inducing factor	\mathcal{T} breaking	Spin-orbit coupling	\mathcal{I} breaking
Boundary mode	Chiral edge states	Helical edge states	Valley kink states
Boundary mode dispersion			

Figure 2.2: Comparisons between different 2D topological phases. Taken from [8]

2.4 Mathematical Formulation of Valley Polarization

To understand the formation of valley-polarized states mathematically, consider the photonic band structure near the K and K' points. The Hamiltonian for a VPC can be approximated near the Dirac points by a mass term M introduced through \mathcal{I} breaking. This mass term opens a bandgap, with each valley exhibiting opposite Berry curvature. The effective Hamiltonian near each valley can be represented as:

$$H_{\text{eff}} = v_D(\sigma_x k_x + \sigma_y k_y) + M\sigma_z,$$

where v_D denotes the Dirac velocity, $\sigma_{x,y,z}$ are Pauli matrices representing the pseudospin in the lattice, and M is the mass term associated with inversion symmetry breaking. The sign of M determines the valley polarization, with opposite signs for the K and K' valleys.

2.5 Topological Protection in Valley Photonic Crystals

One of the most remarkable features of VPCs is their inherent robustness against scattering due to topological protection. This property arises from the **Berry curvature and valley-Chern number associated with each valley**. In a system with \mathcal{I} -breaking but time-reversal symmetry (\mathcal{T}), the Berry curvature, $\Omega(k)$, is nonzero around the valleys and takes opposite values at K and K' . The valley-Chern number C_v can be defined as the integral of the Berry curvature around each valley, given by:

$$C_v = \frac{1}{2\pi} \int_{\text{valley}} \Omega(k) d^2k = \pm \frac{1}{2}.$$

The half-integer value of C_v indicates the **presence of valley-locked topological edge states**, also called **kink states**, that form at domain walls between regions with opposite valley-Chern numbers. These edge states **propagate unidirectionally** and exhibit **minimal backscattering** even in the presence of structural imperfections, as long as there is **no intervalley scattering** between K and K' .

2.6 Practical Example: Waveguiding Applications of VPCs

The practical utility of VPCs is demonstrated most effectively in robust waveguiding applications, where valley-polarized edge states enable defect-tolerant light transmission across complex paths. VPC-based waveguides can maintain single-mode, valley-polarized edge states that are resilient to defects and abrupt bends. This characteristic is advantageous in high-density on-chip photonic circuits, as it ensures reliable data transfer without signal degradation.

For instance, a VPC waveguide constructed from a triangular lattice of dielectric rods can be designed to operate at terahertz frequencies. By manipulating the unit cell geometry, a photonic bandgap can be opened around the Dirac points, allowing for valley-Hall phase propagation. This design enables directional light propagation around sharp corners, as shown in simulations and experiments [9] (see Figure 2.3).

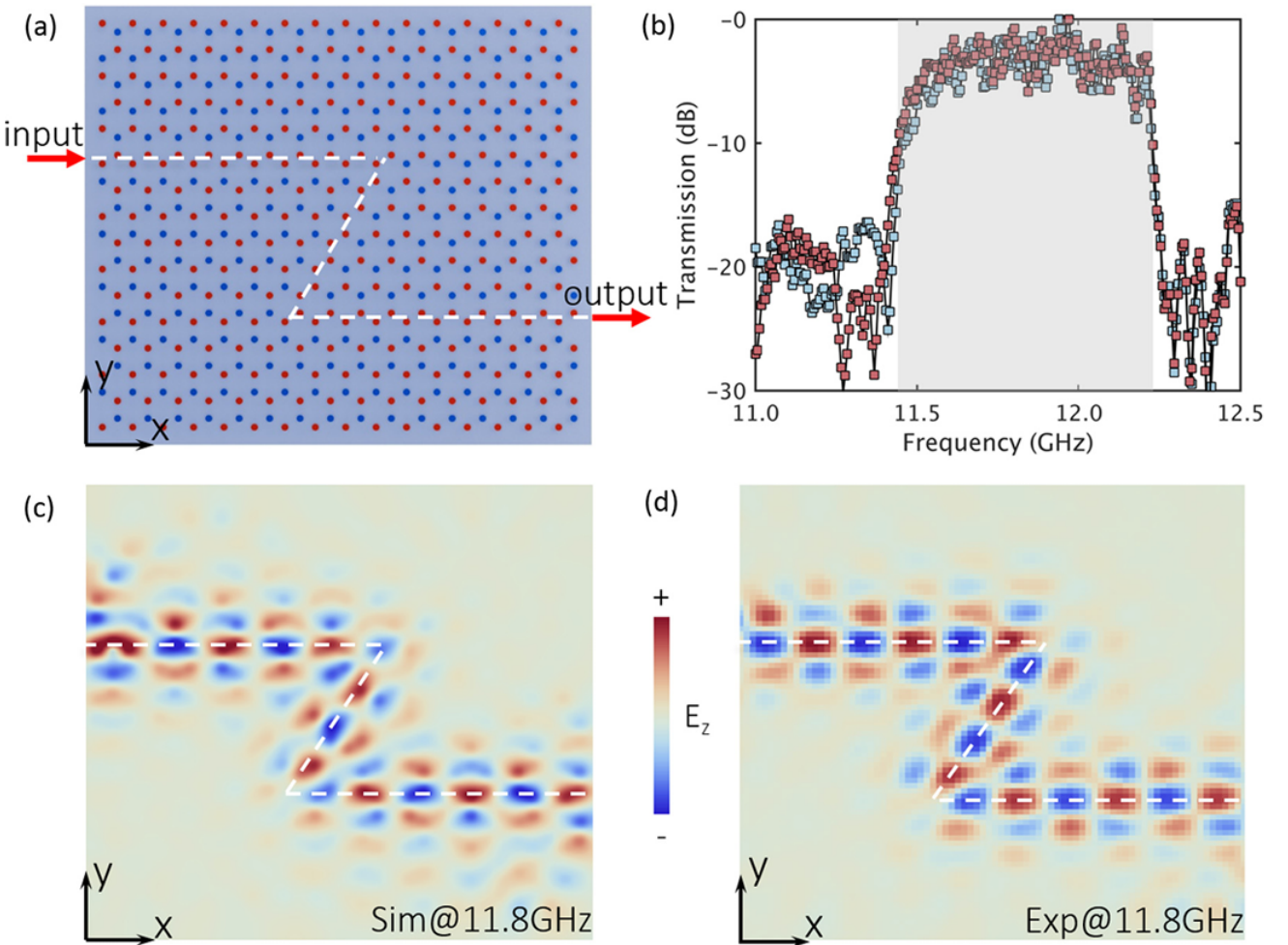


Figure 2.3: VPC waveguiding around a sharp bend with minimal loss. [9]

2.7 Berry Curvature and Chern Numbers in VPCs

The Berry curvature $\Omega_n(k)$ and Chern number C_n are critical parameters in quantifying the topological properties of valley-polarized states. The Berry curvature for a given band n can be expressed as:

$$\Omega_n(k) = \frac{\partial A_y}{\partial k_x} - \frac{\partial A_x}{\partial k_y},$$

where $A_n = -i\langle u_n | \nabla_k | u_n \rangle$ represents the Berry connection, and $|u_n\rangle$ denotes the periodic part of the Bloch wavefunction. The Chern number, representing the integral of Berry curvature over the entire Brillouin zone, is given by:

$$C_n = \frac{1}{2\pi} \int_{\text{BZ}} \Omega_n(k) d^2k.$$

In the case of VPCs, the Chern number for the bulk bands remains zero, while each valley acquires a half-integer valley-Chern number ($\pm\frac{1}{2}$) due to the localized Berry curvature around K and K' . This half-integer nature supports the formation of robust valley-polarized edge states at domain walls, a phenomenon verified through simulations and experimental studies [10] [9] [11] [2].

Chapter 3

Methodology

The Plane Wave Expansion (PWE) method is an established computational approach for analyzing the band structure of photonic crystals, offering an efficient framework to capture the influence of periodic dielectric environments on electromagnetic wave propagation. In this study, we employ the PWE method to compute the photonic band structure of two-dimensional photonic crystals and to further investigate their topological properties. This section describes the theoretical and computational approach taken, including the foundational principles, the steps for computing topological invariants, and the methods used to ensure convergence and accuracy in our results.

The methodology is structured into three primary parts:

1. Mathematical Derivation of the PWE Method:

The PWE method relies on the periodicity of photonic crystals, allowing us to expand both the dielectric function and electromagnetic fields as Fourier series in terms of reciprocal lattice vectors. This derivation begins with Maxwell's equations in the context of a periodic dielectric medium. From these equations, we systematically develop the master equation for the photonic band structure, ultimately casting it as an eigenvalue problem. The eigenvalue solution provides the frequency spectrum for each wave vector, outlining the band structure. This rigorous mathematical foundation forms the basis for accurate and reproducible band structure calculations. Many of the calculations/derivations done here are referenced from [12] [13].

2. Computation of Topological Properties:

Beyond band structure, we are particularly interested in the topological characteristics of the photonic crystal bands, which are quantified by Berry curvature and Chern numbers. These topological invariants provide insight into the robust, defect-tolerant properties of the photonic crystal and are critical for understanding phenomena such as unidirectional edge states. Here, we outline the procedures for calculating Berry curvature using the Berry connection and subsequently integrating the curvature over the Brillouin zone to obtain the Chern number. This part of the methodology builds on the band structure computation, enabling us to analyze the topological phases present in our system.

3. Convergence Testing and Numerical Validation:

To ensure the robustness of our results, we perform detailed convergence tests on key numerical parameters. These tests include assessments of the integration grid density within the Brillouin zone and the number of plane waves used in the Fourier expansion. Such convergence analyses are essential for balancing computational accuracy with efficiency, as higher resolution and more plane waves increase computational demands. In particular, we evaluate the stability of computed Chern numbers with respect to grid density, and we assess the precision of frequency bands under varying plane wave counts. Additionally, a time complexity analysis provides insight into the scaling behavior of our approach, offering a benchmark for selecting optimal parameters in future work.

Each section of this methodology thus builds on the previous, leading from the foundational equations to practical computation and validation. This systematic approach ensures that our findings are both accurate and reproducible, contributing to a deeper understanding of the unique properties of topological photonic crystals.

3.1 Mathematical Derivation of PWE Method for Photonic Crystals

3.1.1 Eigen-equations from Maxwell's Equations

Maxwell's equations in differential form for non-magnetic media:

$$\begin{aligned}\nabla \cdot \mathbf{E} &= \frac{\rho}{\epsilon_0} & \nabla \cdot \mathbf{B} &= 0 \\ \nabla \times \mathbf{E} &= -\frac{\partial \mathbf{B}}{\partial t} & \nabla \times \mathbf{B} &= \mu_0 \mathbf{J} + \mu_0 \epsilon_0 \frac{\partial \mathbf{E}}{\partial t}\end{aligned}\quad (3.1)$$

For a non-magnetic medium: $\mathbf{B}(\mathbf{r}, t) = \mu_0 \mathbf{H}(\mathbf{r}, t)$

For a linear, isotropic medium: $\mathbf{D}(\mathbf{r}, t) = \epsilon_r(\mathbf{r}) \epsilon_0 \mathbf{E}(\mathbf{r}, t)$

Therefore:

$$\begin{aligned}\nabla \times \mathbf{E}(\mathbf{r}, t) &= -\frac{\partial \mu_0 \mathbf{H}(\mathbf{r}, t)}{\partial t} \\ \nabla \times \mathbf{H}(\mathbf{r}, t) &= \frac{\partial \epsilon_r(\mathbf{r}) \epsilon_0 \mathbf{E}(\mathbf{r}, t)}{\partial t}\end{aligned}\quad (3.2)$$

If we operate $(-\nabla \times)$ on Equation (2.1) and substitute $\nabla \times \mathbf{H}(\mathbf{r}, t)$ from Equation (2.2), we get:

$$\nabla \times (\nabla \times \mathbf{E}) = -\mu_0 \epsilon_0 \frac{\partial^2 \mathbf{E}}{\partial t^2}\quad (3.3)$$

In the time-harmonic form, we have:

$$\begin{aligned}\mathbf{E}(\mathbf{r}, t) &= \mathbf{E}_0 e^{i(\mathbf{k} \cdot \mathbf{r} - \omega t)} \\ \frac{\partial \mathbf{E}}{\partial t} &= -i\omega \mathbf{E} \\ \frac{\partial^2 \mathbf{E}}{\partial t^2} &= -\omega^2 \mathbf{E}\end{aligned}\quad (3.4)$$

Thus, we can write the eigen-equation for the \mathbf{E} field as:

$$\boxed{\frac{1}{\epsilon_0} \nabla \times (\nabla \times \mathbf{E}) = -\frac{\omega^2}{c^2} \mathbf{E}}\quad (3.5)$$

If we operate $(-\frac{\nabla \times}{\epsilon_r(\mathbf{r})})$ on Equation (2.2) and substitute $\nabla \times \mathbf{H}(\mathbf{r}, t)$ from Equation (2.1), we get:

$$\nabla \times \left(\frac{1}{\epsilon_r} \nabla \times \mathbf{H} \right) = \epsilon_0 \mu_0 \frac{\partial^2 \mathbf{H}}{\partial t^2}\quad (3.6)$$

In the time-harmonic form, we similarly have:

$$\begin{aligned}\mathbf{H}(\mathbf{r}, t) &= \mathbf{H}_0 e^{i(\mathbf{k} \cdot \mathbf{r} - \omega t)} \\ \frac{\partial \mathbf{H}}{\partial t} &= -i\omega \mathbf{H} \\ \frac{\partial^2 \mathbf{H}}{\partial t^2} &= -\omega^2 \mathbf{H}\end{aligned}\quad (3.7)$$

Thus, we can write the eigen-equation for the \mathbf{H} field as:

$$\boxed{\nabla \times \left(\frac{1}{\epsilon_r} \nabla \times \mathbf{H} \right) = \frac{\omega^2}{\mu_0 c^2} \mathbf{H}}\quad (3.8)$$

3.1.2 Eigen-equation in TE (Transverse Electric) Mode

TE (Transverse Electric) mode in 2D photonic crystals (x-y plane) implies that $H_x = H_y = 0, E_z = 0$ and thus $H_z \neq 0, E_x, E_y \neq 0$.

$$\begin{aligned}\nabla \times \mathbf{E} &= \begin{pmatrix} \frac{\partial}{\partial x} \\ \frac{\partial}{\partial y} \\ \frac{\partial}{\partial z} \end{pmatrix} \times \begin{pmatrix} E_x \\ E_y \\ E_z \end{pmatrix} = \begin{pmatrix} \frac{\partial E_z}{\partial y} - \frac{\partial E_y}{\partial z} \\ \frac{\partial E_x}{\partial z} - \frac{\partial E_z}{\partial x} \\ \frac{\partial E_y}{\partial x} - \frac{\partial E_x}{\partial y} \end{pmatrix}, \\ \nabla \times \mathbf{H} &= \begin{pmatrix} \frac{\partial}{\partial x} \\ \frac{\partial}{\partial y} \\ \frac{\partial}{\partial z} \end{pmatrix} \times \begin{pmatrix} H_x \\ H_y \\ H_z \end{pmatrix} = \begin{pmatrix} \frac{\partial H_z}{\partial y} - \frac{\partial H_y}{\partial z} \\ \frac{\partial H_x}{\partial z} - \frac{\partial H_z}{\partial x} \\ \frac{\partial H_y}{\partial x} - \frac{\partial H_x}{\partial y} \end{pmatrix}.\end{aligned}\quad (3.9)$$

From the curl of \mathbf{E} and \mathbf{H} and the fact that we have $H_x = H_y = 0, E_z = 0$:

$$\begin{aligned}\frac{\partial E_y}{\partial x} - \frac{\partial E_x}{\partial y} &= -\mu_0 \frac{\partial H_z}{\partial t}, \\ \frac{\partial H_z}{\partial y} &= \varepsilon_r \varepsilon_0 \frac{\partial E_x}{\partial t}, \\ \frac{\partial H_z}{\partial x} &= -\varepsilon_r \varepsilon_0 \frac{\partial E_y}{\partial t}.\end{aligned}\quad (3.10)$$

From the previous question, we know that:

$$\nabla \times \left(\left(\frac{1}{\varepsilon_r} \right) (\nabla \times \mathbf{H}) \right) = \frac{\omega^2}{\mu_0 c^2} \mathbf{H} \quad (3.11)$$

Let $\Psi = \frac{1}{\varepsilon_r}$ and $A = \nabla \times \mathbf{H}$

Using the vector identity for the curl of a product of a scalar field ψ and a vector field \mathbf{A} , we have:

$$\nabla \times (\psi \mathbf{A}) = \psi (\nabla \times \mathbf{A}) + (\nabla \psi) \times \mathbf{A} \quad (3.12)$$

And for the curl of the curl of a vector field \mathbf{A} , the identity is:

$$\nabla \times (\nabla \times \mathbf{A}) = \nabla (\nabla \cdot \mathbf{A}) - \nabla^2 \mathbf{A} \quad (3.13)$$

$$\begin{aligned}\nabla \times (\psi \mathbf{A}) &= \psi \nabla \times \mathbf{A} + (\nabla \psi) \times \mathbf{A} \\ &= \psi (\nabla \times (\nabla \times \mathbf{H})) + ((\nabla \psi) \times (\nabla \times \mathbf{H})) \\ &= \psi (\nabla (\nabla \cdot \mathbf{H}) - \nabla^2 \mathbf{H}) + ((\nabla \psi) \times (\nabla \times \mathbf{H}))\end{aligned}\quad (3.14)$$

The first two terms on the RHS of Equation (14) are zero (First term zero due to Maxwell's Equations and Second Term zero due to Assumptions)

$$\nabla \times \left(\frac{1}{\varepsilon_n} (\nabla \times \mathbf{H}) \right) = \begin{pmatrix} i & j & k \\ \frac{\partial}{\partial x} \left(\frac{1}{\varepsilon_r} \right) & \frac{\partial}{\partial y} \left(\frac{1}{\varepsilon_r} \right) & \frac{\partial}{\partial z} \left(\frac{1}{\varepsilon_r} \right) \\ \frac{\partial H_z}{\partial y} & -\frac{\partial H_z}{\partial x} & 0 \end{pmatrix}$$

$$\boxed{\nabla \times \left(\frac{1}{\varepsilon_n} (\nabla \times \mathbf{H}) \right) = \left(\frac{\partial}{\partial x} \left(\frac{1}{\varepsilon_n} \frac{\partial H_z}{\partial x} \right) + \frac{\partial}{\partial y} \left(\frac{1}{\varepsilon_n} \frac{\partial H_z}{\partial y} \right) \right) H_z = \frac{\omega^2}{c^2} H_z} \quad (3.15)$$

Assumption is that there is no permittivity variation of the photonic crystal in the z-direction and that electromagnetic field variation is also absent in the z-direction.

3.1.3 Inverse Dielectric Function and Field Eigenstates

The Helmholtz equations in the time-harmonic form can be written as:

$$-\frac{1}{\varepsilon(\mathbf{r})} \nabla \times (\nabla \times \mathbf{E}(\mathbf{r})) = \frac{\omega^2}{c^2} \mathbf{E}(\mathbf{r}), \quad (3.16)$$

$$\nabla \times \left(\frac{1}{\varepsilon(\mathbf{r})} \nabla \times \mathbf{H}(\mathbf{r}) \right) = \frac{\omega^2}{c^2} \mathbf{H}(\mathbf{r}), \quad (3.17)$$

where \mathbf{r} is a 3D vector in coordinate space.

Since we are searching for eigen-states of infinite periodic structure, spatial distribution of the field components \mathbf{E} and \mathbf{h} may be represented in the form of Bloch functions, namely, the plane waves multiplied by periodic function with periodicity of lattice:

$$\mathbf{E}(\mathbf{r}) = \mathbf{E}_{\mathbf{k},n}(\mathbf{r}) \cdot e^{i\mathbf{k}\cdot\mathbf{r}}, \quad (3.18)$$

$$\mathbf{H}(\mathbf{r}) = \mathbf{H}_{\mathbf{k},n}(\mathbf{r}) \cdot e^{i\mathbf{k}\cdot\mathbf{r}}, \quad (3.19)$$

where $\mathbf{E}_{\mathbf{k},n}$ and $\mathbf{H}_{\mathbf{k},n}$ are periodic functions with the periodicity of the lattice, satisfying the conditions:

$$\mathbf{E}_{\mathbf{k},n}(\mathbf{r} + \mathbf{R}) = \mathbf{E}_{\mathbf{k},n}(\mathbf{r}), \quad (3.20)$$

$$\mathbf{H}_{\mathbf{k},n}(\mathbf{r} + \mathbf{R}) = \mathbf{H}_{\mathbf{k},n}(\mathbf{r}), \quad (3.21)$$

for any lattice vector \mathbf{R} . However, periodicity of wave functions leads to possibility of their Fourier expansion over reciprocal lattice vectors \mathbf{G} . Thus, we can represent the wave function in wave vectors space instead of coordinate space:

$$\mathbf{E}_{\mathbf{k},n}(\mathbf{r}) = \sum_{\mathbf{G}} \mathbf{E}'_{\mathbf{k},n}(\mathbf{G}) \exp(i(\mathbf{k} + \mathbf{G}) \cdot \mathbf{r})$$

$$\mathbf{H}_{\mathbf{k},n}(\mathbf{r}) = \sum_{\mathbf{G}} \mathbf{H}'_{\mathbf{k},n}(\mathbf{G}) \exp(i(\mathbf{k} + \mathbf{G}) \cdot \mathbf{r})$$

(3.22)

The dielectric function can also be expanded into a Fourier series due to the periodicity:

$$\frac{1}{\varepsilon(\mathbf{r})} = \sum_{\mathbf{G}} \chi(\mathbf{G}) \cdot \exp(i\mathbf{G} \cdot \mathbf{r})$$

(3.23)

where $\chi(\mathbf{G})$ are the Fourier expansion coefficients which depend on the reciprocal lattice vectors.

For 2D Photonic Crystals

The Fourier expansion coefficients of the dielectric function in a 2D PhC and the corresponding eigenvalue equations for the Fourier expansion coefficients of electric and magnetic fields are derived from the periodicity of the wave functions and the Bloch theorem.

The lattice translation vectors and reciprocal lattice vectors in a 2D photonic crystal are given by:

$$\mathbf{R}_n = n_1 \mathbf{a}_1 + n_2 \mathbf{a}_2,$$

$$\mathbf{G}_m = m_1 \mathbf{b}_1 + m_2 \mathbf{b}_2,$$

where $G_{mn} \cdot R = 2\pi N$ and m, n, N are integers.

The permittivity and the magnetic field solutions (eigenstates) of 2D photonic crystals can be expressed as the following Fourier series (sum of plane waves):

$$\frac{1}{\varepsilon_r(\mathbf{r})} = \sum_m \chi(\mathbf{G}_m) \exp(i\mathbf{G}_m \cdot \mathbf{r}), \quad (3.24)$$

$$H_{z,\mathbf{k}_{||}}(\mathbf{r}) = \sum_m H_{z,\mathbf{k}_{||}m}(\mathbf{G}_m) \exp(i(\mathbf{k}_{||} + \mathbf{G}_m) \cdot \mathbf{r}), \quad (3.25)$$

where M is the total number of plane waves, $\chi(\mathbf{G}_m)$ are the Fourier coefficients of permittivity function, $\mathbf{k}_{||}$ are propagation wave vectors of the magnetic field, and $H_{z,\mathbf{k}_{||}m}(\mathbf{G}_m)$ are the complex amplitude coefficients of the magnetic field.

3.1.4 Master Equation, Eigenmatrix Construction in 2D PhCs

We derived the reduced form of Maxwell's microscopic equations for TE mode ($H_x = H_y = E_z = 0$) in 2D-photonic crystals (xy-plane).

$$-\left[\frac{\partial}{\partial x} \left(\frac{1}{\varepsilon_r} \frac{\partial}{\partial x} \right) + \frac{\partial}{\partial y} \left(\frac{1}{\varepsilon_r} \frac{\partial}{\partial y} \right) \right] H_z = \frac{\omega^2}{c^2} H_z \quad (3.26)$$

We also expressed the inverse permittivity function $\left(\frac{1}{\varepsilon_n}\right)$ and Magnetic field solutions (H_z) as Fourier series:

$$\frac{1}{\varepsilon_n(\mathbf{r})} = \sum_m \chi(\mathbf{G}_m) \exp(i\mathbf{G}_m \cdot \mathbf{r}) \quad (3.27)$$

$$H_{z,\mathbf{k}_{||}}(\mathbf{r}) = \sum_m H_{z,\mathbf{k}_{||}m}(\mathbf{G}_m) \exp(i(\mathbf{k}_{||} + \mathbf{G}_m) \cdot \mathbf{r}) \quad (3.28)$$

where $\mathbf{r} \rightarrow (x, y)$, $\mathbf{G} \rightarrow (G_x, G_y)$, $\mathbf{k}_{||} \rightarrow (k_{x_{||}}, k_{y_{||}})$

Substituting (2) and (3) in (1):

$$\begin{aligned} & \sum_{m'} \frac{\partial}{\partial x} \chi(\mathbf{G}_{m'}) \exp(iG_x^{(m')}x) \exp(iG_y^{(m')}y) \sum_m \frac{\partial}{\partial x} H_{z,\mathbf{k}_{||}m'}(\mathbf{G}_m) \\ & \quad \times \exp(i(k_{x_{||}}x + G_x^{(m')}x)) \exp(i(k_{y_{||}}y + G_y^{(m')}y)) + \\ & \sum_{m'} \frac{\partial}{\partial y} \chi(\mathbf{G}_{m'}) \exp(iG_x^{(m')}x) \exp(iG_y^{(m')}y) \sum_m \frac{\partial}{\partial y} H_{z,\mathbf{k}_{||}m'}(\mathbf{G}_m) \\ & \quad \times \exp(i(k_{x_{||}}x + G_x^{(m')}x)) \exp(i(k_{y_{||}}y + G_y^{(m')}y)) + \\ & \frac{\omega^2}{c^2} \sum_m H_{z,\mathbf{k}_{||}m}(\mathbf{G}_m) \exp(i(k_{x_{||}}x + G_x^{(m)}x) + i(k_{y_{||}}y + G_y^{(m)}y)) = 0 \end{aligned} \quad (3.29)$$

Taking into account that $\mathbf{G} = \mathbf{G}' + \mathbf{G}''$, with $\mathbf{G}'' = \mathbf{G} - \mathbf{G}'$, reducing the first two terms to common

summation:

$$\begin{aligned}
& \sum_m \sum_{m'} \frac{\partial}{\partial x} \chi(\mathbf{G}_m - \mathbf{G}_{m'}) \exp[i((\mathbf{G}_m - \mathbf{G}_{m'})x + (\mathbf{G}_m - \mathbf{G}_{m'})y)] H_{z,\mathbf{k}_\parallel m'}(\mathbf{G}_m) \\
& \quad \times \frac{\partial}{\partial x} \exp[i((k_{x_\parallel} x + G_x^{(m')} x) + (k_{y_\parallel} y + G_y^{(m')} y))] + \\
& \sum_m \sum_{m'} \frac{\partial}{\partial y} \chi(\mathbf{G}_m - \mathbf{G}_{m'}) \exp[i((\mathbf{G}_m - \mathbf{G}_{m'})x + (\mathbf{G}_m - \mathbf{G}_{m'})y)] H_{z,\mathbf{k}_\parallel m'}(\mathbf{G}_m) \\
& \quad \times \frac{\partial}{\partial y} \exp[i((k_{x_\parallel} x + G_x^{(m')} x) + (k_{y_\parallel} y + G_y^{(m')} y))] + \\
& \frac{\omega^2}{c^2} \sum_m H_{z,\mathbf{k}_\parallel m}(\mathbf{G}_m) \exp[i((k_{x_\parallel} x + G_x^{(m)} x) + (k_{y_\parallel} y + G_y^{(m)} y))] = 0
\end{aligned} \tag{3.30}$$

Taking derivatives and combining exponents:

$$\begin{aligned}
& \sum_m \sum_{m'} \chi(\mathbf{G}_m - \mathbf{G}_{m'}) H_{z,\mathbf{k}_\parallel m'}(\mathbf{G}_{m'}) \exp \left[i(k_x x + k_y y + G_x^{(m')} x + G_y^{(m')} y) \right] \\
& \quad \times i(k_x + G_x^{(m)}) \times i(k_x + G_x^{(m')}) + \\
& \sum_m \sum_{m'} \chi(\mathbf{G}_m - \mathbf{G}_{m'}) H_{z,\mathbf{k}_\parallel m'}(\mathbf{G}_{m'}) \exp \left[i(k_x x + k_y y + G_x^{(m')} x + G_y^{(m')} y) \right] \\
& \quad \times i(k_y + G_y^{(m)}) \times i(k_y + G_y^{(m')}) + \\
& \frac{\omega^2}{c^2} \sum_m H_{z,\mathbf{k}_\parallel m}(\mathbf{G}_m) \exp \left[i(k_x x + k_y y + G_x^{(m)} x + G_y^{(m)} y) \right] = 0
\end{aligned} \tag{3.31}$$

We can simplify the above using the relations below:

$$\begin{aligned}
(k_x + G_x^{(m)}) \times (k_x + G_x^{(m')}) + (k_y + G_y^{(m)}) \times (k_y + G_y^{(m')}) &= (\mathbf{k}_\parallel + \mathbf{G}^{(m)}) \cdot (\mathbf{k}_\parallel + \mathbf{G}^{(m')}) \\
(k_x x + k_y y + G_x^{(m)} x + G_y^{(m)} y) &= (\mathbf{k}_\parallel + \mathbf{G}^{(m)}) \cdot \mathbf{r}
\end{aligned}$$

Now, projecting the above equation to the basis $\exp[i((\mathbf{k}_\parallel + \mathbf{G}_{m'}) \cdot \mathbf{r})]$ gives the Master Equation:

$$\sum_{m'} \chi(\mathbf{G}_m - \mathbf{G}_{m'}) [(\mathbf{k}_\parallel + \mathbf{G}_m) \cdot (\mathbf{k}_\parallel + \mathbf{G}_{m'})] H_{z,\mathbf{k}_\parallel m'}(\mathbf{G}_m) = \frac{\omega^2}{c^2} H_{z,\mathbf{k}_\parallel m}(\mathbf{G}_m)$$

The use of different indices (m, m', m'') allows us to distinguish between the various components of the Fourier series expansions. Since we're dealing with a periodic structure, these indices help us keep track of the different harmonic components in the reciprocal lattice vector space. They represent different orders of the harmonics in the expansion.

The relation $\mathbf{G} = \mathbf{G}' + \mathbf{G}''$ originates from the fact that in a periodic system, the reciprocal lattice vectors are defined by the sum or difference of other reciprocal lattice vectors due to the periodic boundary conditions. This property is inherent in the discrete translational symmetry of a crystalline structure and is crucial when computing the band structure, as it ensures that the wavefunctions have the same periodicity as the lattice.

Eigenmatrix Construction

The master equation for the band structure computation of 2D photonic crystals (PhC) is similar to that of 1D PhC, with adjustments made for dimensionality. The master equation is given by:

$$\sum_{m'} \chi(\mathbf{G}_m - \mathbf{G}_{m'}) [(\mathbf{k}_\parallel + \mathbf{G}_m) \cdot (\mathbf{k}_\parallel + \mathbf{G}_{m'})] H_{z,\mathbf{k}_\parallel m'}(\mathbf{G}_m) = \frac{\omega^2}{c^2} H_{z,\mathbf{k}_\parallel m}(\mathbf{G}_m) \tag{3.33}$$

where χ is the Fourier coefficient, k is the wave vector, G and G' are reciprocal lattice vectors, and ω is the angular frequency of light. This equation is known as the "Master equation" for 2D PhC. For 2D photonic crystals, the wave vector k and the reciprocal lattice vectors G become two-dimensional vectors denoted as k_{\parallel} and \mathbf{G} . The dot product is used in place of the normal product which is used in 1D PhC.

The differential operator in the master equation is represented in a matrix form, whose element can be found using the expression:

$$\hat{\Theta}_{G,G'} = \chi(\mathbf{G} - \mathbf{G}')[(\mathbf{k}_{\parallel} + \mathbf{G}) \cdot (\mathbf{k}_{\parallel} + \mathbf{G}')] \quad (3.34)$$

The set of solutions for the equation system can be found as eigenvalues of the matrix differential operator, which has the form:

$$\hat{\Theta} = \begin{bmatrix} \hat{\Theta}_{G_1,G_1} & \hat{\Theta}_{G_2,G_1} & \cdots & \hat{\Theta}_{G_N,G_1} \\ \hat{\Theta}_{G_1,G_2} & \hat{\Theta}_{G_2,G_2} & \cdots & \hat{\Theta}_{G_N,G_2} \\ \vdots & \vdots & \ddots & \vdots \\ \hat{\Theta}_{G_1,G_N} & \hat{\Theta}_{G_2,G_N} & \cdots & \hat{\Theta}_{G_N,G_N} \end{bmatrix} \quad (3.35)$$

This matrix is constructed such that the set of G vectors must be the same as G' vectors, ensuring the matrix is square. The eigenvalues of this matrix correspond to the allowed frequencies of the photonic crystal modes.

3.1.5 Fourier Coefficients

The Fourier expansion of the dielectric function in a photonic crystal is given by the expression in previous questions which relates the inverse permittivity function $\epsilon_r(\mathbf{r})$ to a Fourier series over the reciprocal lattice vectors \mathbf{G} :

$$\frac{1}{\epsilon_r(\mathbf{r})} = \sum_{\mathbf{G}} \chi(\mathbf{G}) \exp(i\mathbf{G} \cdot \mathbf{r}) \quad (3.1)$$

The Fourier expansion coefficients $\chi(\mathbf{G})$ for the inverse dielectric function can be calculated using the following integral over the unit cell of the photonic crystal:

$$\chi(\mathbf{G}) = \frac{1}{V_0} \int_{V_0} \frac{1}{\epsilon_r(\mathbf{r})} \exp(-i\mathbf{G} \cdot \mathbf{r}) d\mathbf{r} \quad (3.2)$$

For the case of **2D photonic crystals** the expression for $\chi(\mathbf{G})$ can be simplified to:

$$\chi(\mathbf{G}_{\parallel}) = \frac{1}{V_0^{(2)}} \int_{V_0^{(2)}} \frac{1}{\epsilon_r(\mathbf{r}_{\parallel})} \exp(-i\mathbf{G}_{\parallel} \cdot \mathbf{r}_{\parallel}) d\mathbf{r}_{\parallel} \quad (3.3)$$

Here, $V_0^{(2)}$ is the area of the 2D photonic crystal unit cell, and the integration is performed over the unit cell in the plane of the photonic crystal.

Note: The above equations will provide an exact representation when the system has perfect and infinite periodicity. Though for numerical methods, the Fourier series is truncated at a sufficient number of terms to capture the variation in the dielectric function and the magnetic field distribution.

To solve for the Fourier expansion coefficients numerically, one can discretize the unit cell into a mesh and approximate the integral by a summation. The discretization process involves creating a mesh over the unit cell and evaluating the permittivity at each mesh point. The Fourier coefficients are then given by:

$$\begin{aligned}
\chi(\mathbf{G}_{||}) &= \frac{1}{V_0^{(2)}} \int_{V_0^{(2)}} \frac{1}{\varepsilon(\mathbf{r}_{||})} \exp(-i\mathbf{G}_{||} \cdot \mathbf{r}_{||}) d\mathbf{r}_{||} \\
&= \frac{1}{a \cdot b} \iint \frac{1}{\varepsilon(x, y)} \exp(i(G_x x + G_y y)) dx dy \\
&= \frac{1}{a \cdot b} \sum_{j=0}^{N_x} \sum_{k=0}^{N_y} \frac{1}{\varepsilon(x_j, y_k)} \exp(i(G_x x_j + G_y y_k)) \Delta x_j \cdot \Delta y_k
\end{aligned} \tag{3.4}$$

where a and b are the dimensions of the unit cell in the x and y directions, N_x and N_y are the numbers of mesh nodes in the x and y directions, Δx and Δy are the dimensions of each mesh cell, and $\epsilon(x_j, y_k)$ is the value of the permittivity function at the mesh point with coordinates (x_j, y_k) .

This numerical method allows for the computation of the Fourier expansion coefficients even when the dielectric function has a complex geometry that does not permit an analytical solution. It is seen that growth of the mesh element number leads to inessential growth of the function quality while neither shape nor permittivity values of the function change. Thus, after the validation is finished, we can conclude that number of plane waves is the only crucial factor which determines the shape of the synthesized function. The number of mesh elements in this case is not so important while the mesh cell is small enough to provide good discretization. However, it is necessary to remember that large number of plane waves can dramatically increase computation time.

3.2 Computation of Topological Properties

For the Computation of Berry Curvatures and Chern Numbers, we need to discretize the equations mentioned in the above sections based on our problem. We can do it in the following manner for TE modes of Band Structure of Photonic Crystals:

$$\begin{aligned}
\text{Chern number: } c_n &= \frac{1}{2\pi} \iint \mathbf{F}(\mathbf{k}) \cdot d^2\mathbf{k} = \frac{1}{2\pi} \sum_{k_x, k_y} F(k_x, k_y) \Delta k_x \Delta k_y \\
\text{Berry Curvature: } F(k_x, k_y) &= \nabla_{\mathbf{k}} \times \mathbf{A}(k_x, k_y) = \frac{\Delta A_y(k_x, k_y)}{\Delta k_x} - \frac{\Delta A_x(k_x, k_y)}{\Delta k_y} \\
\text{Berry Connection: } A_\mu(k_x, k_y) &= -i \langle \psi(k_x, k_y) | \nabla_{k_\mu} \psi(k_x, k_y) \rangle = -i \frac{\int H_{z, k_{||}}^+(x, y) \frac{\Delta H_{z, k_{||}}(x, y)}{\Delta k_\mu} dx dy}{\int H_{z, k_{||}}^+(x, y) H_{z, k_{||}}(x, y) dx dy} \\
\text{Magnetic Field: } H_{z, k_{||}}(\mathbf{r}_{||}) &= \sum_{\mathbf{G}_{||}} H_{z, k_{||} n}(\mathbf{G}_{||}) e^{i(k_{||} + \mathbf{G}_{||}) \cdot \mathbf{r}_{||}}
\end{aligned} \tag{3.36}$$

3.3 Computation of Electric and Magnetic Fields

Starting with Maxwell's curl equation for the magnetic field:

$$\nabla \times \mathbf{H}(\mathbf{r}, t) = \frac{\partial(\varepsilon_r(\mathbf{r})\varepsilon_0 \mathbf{E}(\mathbf{r}, t))}{\partial t} \quad (3.37)$$

We assume a time-harmonic solution for the electric field:

$$\mathbf{E}(\mathbf{r}, t) = \mathbf{E}_0 e^{i(\mathbf{k} \cdot \mathbf{r} - \omega t)} \quad (3.38)$$

Differentiating with respect to time:

$$\frac{\partial \mathbf{E}}{\partial t} = -i\omega \mathbf{E} \quad (3.39)$$

Substituting this into the Maxwell equation:

$$\nabla \times \mathbf{H} = -i\omega \varepsilon_r(\mathbf{r}) \varepsilon_0 \mathbf{E} \quad (3.40)$$

Solving for \mathbf{E} :

$$\mathbf{E} = \frac{\nabla \times \mathbf{H}}{-i\omega \varepsilon_r(\mathbf{r}) \varepsilon_0} \quad (3.41)$$

For the **TE mode** (Transverse Electric mode), the electric field has only in-plane components $\mathbf{E} = (E_x, E_y, 0)$, while the magnetic field has only the **out-of-plane component** (H_z). Given the magnetic field expansion:

$$H_{z,k_{||}}(\mathbf{r}_{||}) = \sum_{\mathbf{G}_{||}} H_{z,k_{||}n}(\mathbf{G}_{||}) e^{i(k_{||} + \mathbf{G}_{||}) \cdot \mathbf{r}_{||}} \quad (3.42)$$

we use Maxwell's equation:

$$\nabla \times \mathbf{H} = -i\omega \varepsilon_r(\mathbf{r}) \varepsilon_0 \mathbf{E} \quad (3.43)$$

In two-dimensional photonic crystals, the curl equations in the Fourier-expanded form give:

$$\mathbf{E}_{||}(\mathbf{r}_{||}) = \frac{1}{i\omega \varepsilon_r(\mathbf{r}) \varepsilon_0} (\hat{z} \times \nabla_{||} H_z(\mathbf{r}_{||})) \quad (3.44)$$

Expanding in terms of plane waves:

$$\mathbf{E}_{||,k_{||}}(\mathbf{r}_{||}) = \sum_{\mathbf{G}_{||}} \frac{\hat{z} \times (k_{||} + \mathbf{G}_{||})}{\omega \varepsilon_r(\mathbf{r}) \varepsilon_0} H_{z,k_{||}n}(\mathbf{G}_{||}) e^{i(k_{||} + \mathbf{G}_{||}) \cdot \mathbf{r}_{||}} \quad (3.45)$$

3.4 Poynting Vector and Power Flow

In a time-harmonic electromagnetic field, the instantaneous Poynting vector is given by:

$$\mathbf{S} = \mathbf{E} \times \mathbf{H} \quad (3.46)$$

To obtain the time-averaged Poynting vector, we compute:

$$\langle \mathbf{S} \rangle = \frac{1}{2} \Re(\mathbf{E} \times \mathbf{H}^*) \quad (3.47)$$

where:

- \mathbf{S} is the **Poynting vector** representing energy flux density.
- \mathbf{E} is the electric field.
- \mathbf{H} is the magnetic field.
- $*$ denotes the complex conjugate.
- $\Re(\cdot)$ represents the real part of the expression.

This equation describes the net power flow per unit area in a photonic crystal, averaged over many periods.

3.5 Convergence Testing

In this section, we present the convergence analysis of several key properties of the photonic crystal system modeled using the Plane Wave Expansion (PWE) method. The aim is to ensure that the computational results, such as band structures and topological invariants (Berry curvature and Chern numbers), are robust and independent of the choice of numerical parameters. We focus on convergence with respect to the number of plane waves, the integration area for computing Chern numbers, and the discretization of the Brillouin zone.

3.5.1 Convergence with Number of Plane Waves

In the Plane Wave Expansion (PWE) method for photonic crystal modeling, the number of plane waves refers to the number of reciprocal lattice vectors \mathbf{G} used in the Fourier expansion of the dielectric function and electromagnetic fields. The total number of plane waves is determined by a parameter n_G , which sets the limit for the reciprocal lattice vectors along each direction. In a two-dimensional (2D) photonic crystal, the total number of plane waves used in the expansion can be expressed as:

$$N_{\text{plane waves}} = (2 \cdot n_G + 1)^2,$$

where n_G is the maximum integer value for reciprocal lattice vectors along each direction.

Increasing the number of plane waves improves the accuracy of the Fourier series representation, providing a more accurate solution to the master equation. However, a larger number of plane waves also increases the size of the eigenvalue problem, which can lead to greater computational costs. Thus, selecting an appropriate number of plane waves involves balancing computational efficiency with the desired level of accuracy.

To test the convergence of the PWE method, we conducted simulations for a well-established photonic crystal structure, as described in Yang et al. [2]. The convergence criteria include the calculated band structure, Berry curvature, and Chern numbers. By gradually increasing n_G , we observed the effect on the resulting band diagrams and topological properties. The structure of the VPC unit cell studied is attached below.

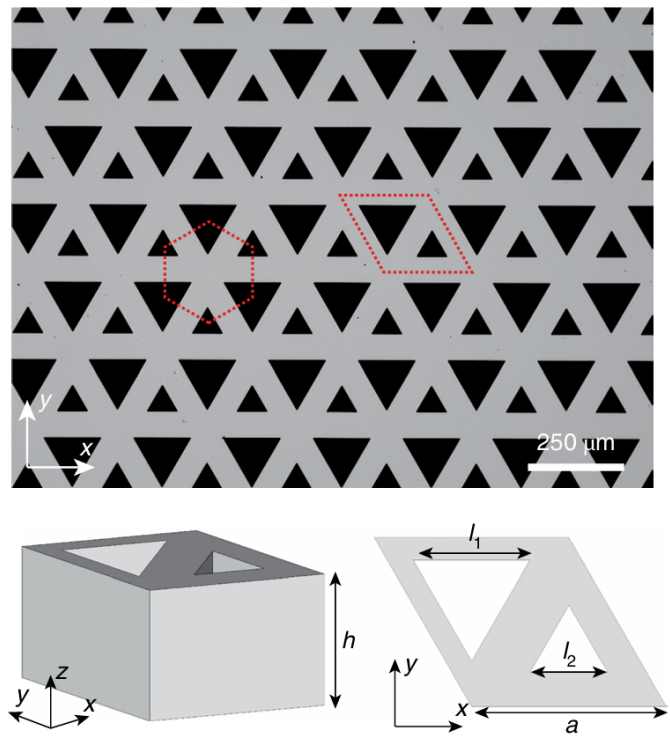


Figure 3.1: The VPC Structure as described in Yang et al. [2]. $l_1 = 0.65a$ and $l_2 = 0.35a$ here.

Band Structure Convergence

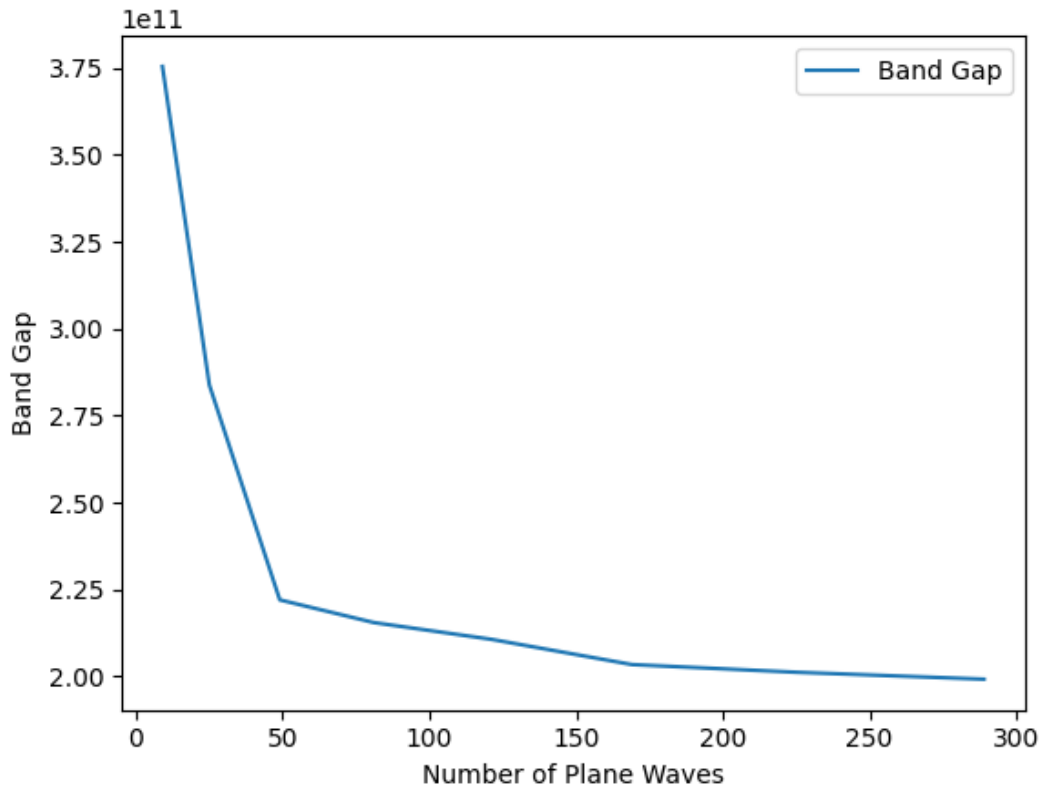


Figure 3.2: Convergence of band structure with increasing number of plane waves. The Band Gap Value stabilizes as n_G increases, particularly after $n_G = 3$.

The band structure was computed for different values of n_G , and the convergence was monitored by comparing the frequency values at key points in the Brillouin zone (e.g., Γ , K , M points). The convergence was deemed satisfactory when the frequency values remained stable (within a predefined tolerance) as n_G increased. From the plot attached below, we can clearly see that $n_G=3$ (Number of Plane Waves = 49) is satisfactory enough for the convergence of Band Structure, and strikes a good balance between time complexity and accuracy.

Berry Curvature and Chern Number Convergence

We also analyzed the convergence of Berry curvature and the resulting Chern number as a function of n_G . As the number of plane waves increased, the Berry curvature distributions at the K and K' valleys showed improved smoothness, indicating better resolution of the topological features of the photonic bands. The Chern number was calculated by integrating the Berry curvature over the Brillouin zone, and convergence was achieved when the computed Chern number became stable with increasing n_G .

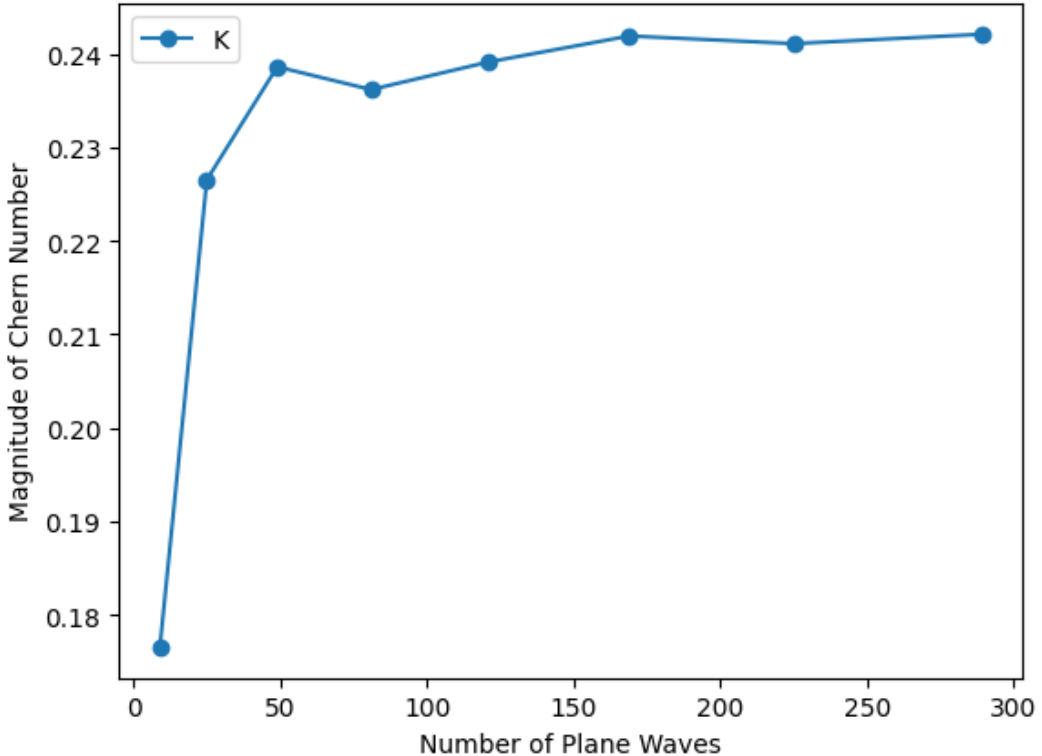


Figure 3.3: Convergence of the Valley Chern Number with increasing number of plane waves. The magnitude of the Valley Chern Number stabilizes as n_G ($n_G = 3$ is satisfactory) increases.

3.5.2 Convergence of Chern Number with Integration Area

The computation of the Chern number involves integrating the Berry curvature over the Brillouin zone. In this analysis, we examined the effect of varying the integration area on the calculated Chern number. Specifically, we tested the convergence of the Chern number by using different sizes of triangular integration areas, ranging from small areas to areas covering half of the Brillouin zone.

The Valley Chern number C_n is defined as:

$$C_n = \frac{1}{2\pi} \int_A \Omega_n(\mathbf{k}) d^2\mathbf{k}, \quad (3.48)$$

where $\Omega_n(\mathbf{k})$ is the Berry curvature for band n . The integration area A was varied systematically, while respecting the symmetry of the Brillouin Zone, and the corresponding Chern number was plotted as a function of the side length of the triangular integration area.

The results showed that the Chern number converged as the integration area approached half of the Brillouin zone as can be seen in Figure 3.4.

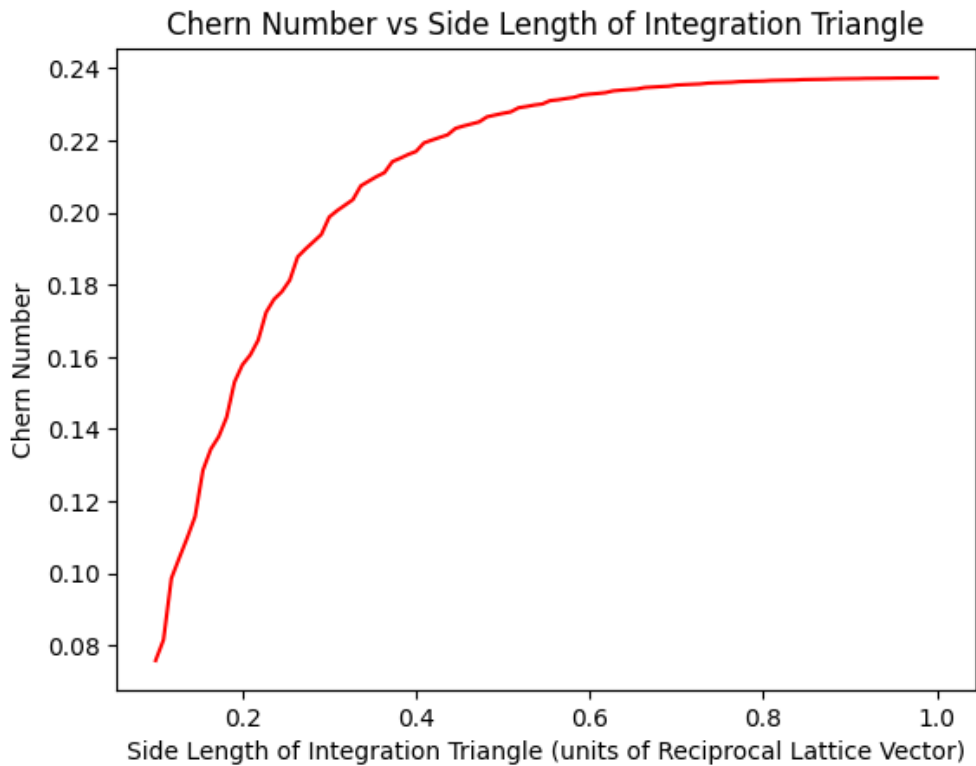


Figure 3.4: Convergence of the Chern number with respect to the integration area. The Chern number stabilizes as the triangular integration area approaches half of the Brillouin zone (When Side Length = Length of Reciprocal Lattice Vectors).

3.5.3 Convergence with Discretization of the Brillouin Zone

The discretization of the Brillouin zone is another factor that affects the accuracy of the computed topological invariants. In this part of the convergence analysis, we tested the effect of varying the number of mesh points used to discretize the Brillouin zone on the calculated Valley Chern number (or Band Gap).

The Berry curvature was evaluated at each mesh point, and the Valley Chern number was obtained by summing the Berry curvature values across the integration area of Half Brillouin Zone (HBZ) over the K and K' valley points:

$$C_n \approx \frac{1}{2\pi} \sum_{HBZ} \Omega_n(k_x, k_y) \Delta k_x \Delta k_y. \quad (3.49)$$

The convergence was assessed by increasing the number of mesh points and monitoring the stability of the Chern number. The results indicated that a finer discretization of the Brillouin zone did not affect the value of Chern Number by much. Increasing the number of mesh points increases the computational cost as $\mathcal{O}(N)$. However, with respect to N_{BZ} , the computational cost scales as $\mathcal{O}(N^2)$. The tradeoff in accuracy does not justify increasing the discretization beyond $N_{BZ} = 25$ as can be clearly seen in Figure 3.5.

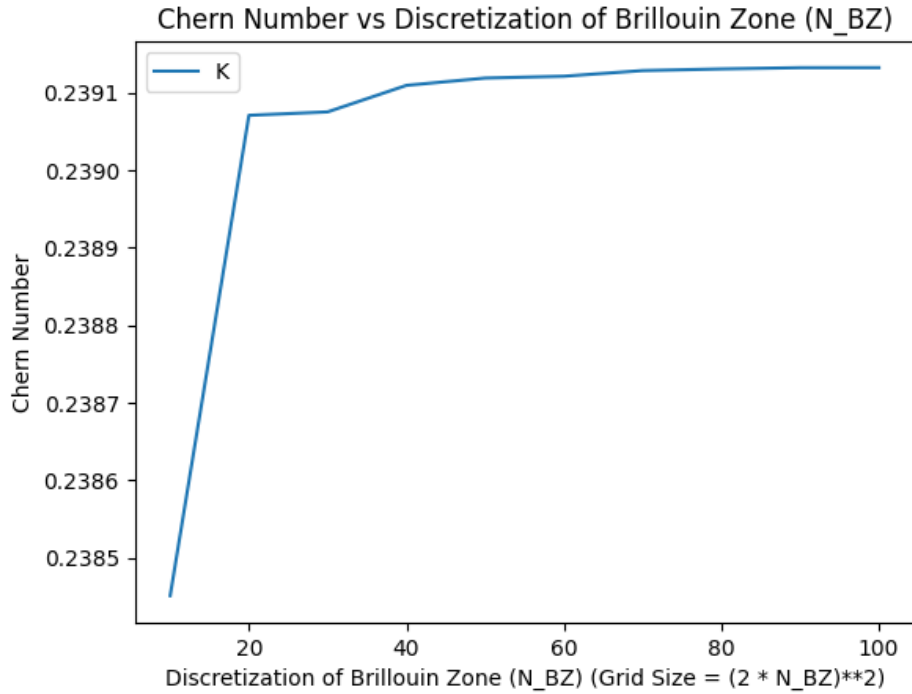


Figure 3.5: Convergence of the Chern number with increasing discretization of the Brillouin zone. The Chern number becomes stable as the number of mesh points increases.

3.5.4 Summary of Convergence Testing

The convergence tests presented in this section provide a comprehensive evaluation of the numerical stability of the PWE method for photonic crystal modeling. By systematically varying the number of plane waves, the integration area, and the discretization of the Brillouin zone, we ensured that the computed band structures, Berry curvatures, and Chern numbers were accurate and independent of the specific numerical parameters chosen. This convergence analysis is crucial for establishing confidence in the robustness of our results and provides guidelines for selecting optimal computational parameters in future studies.

Chapter 4

Optimization Results and Methodology

In this section, we present the optimization strategies employed to enhance the performance of photonic crystal structures, with a primary focus on Bayesian Optimization (BO). The goal of this optimization process is to systematically explore design parameters to maximize the desired figure of merit, which includes maximizing the bandgap, enhancing topological robustness, and minimizing bending losses. This section elaborates on the principles of Bayesian Optimization, explains its time complexity, justifies the chosen figure of merit, and presents the optimization results with supporting figures.

4.1 Introduction to Bayesian Optimization

Bayesian Optimization (BO) is a probabilistic model-based optimization method, especially useful for optimizing expensive-to-evaluate functions. It is highly efficient in exploring high-dimensional parameter spaces and is particularly well-suited for photonic crystal simulations, where each evaluation involves computationally intensive band structure calculations and topological analyses.

BO utilizes a surrogate model, typically a Gaussian Process (GP), to approximate the underlying objective function. By balancing exploration (investigating new areas of the parameter space) and exploitation (focusing on regions known to yield high values), BO can effectively identify optimal solutions with fewer iterations compared to traditional optimization methods.

The Bayesian Optimization workflow used in this study involves the following steps:

1. **Initialization:** A set of initial points is sampled using a Sobol sequence, providing a diverse coverage of the parameter space. These initial evaluations serve as the training data for the GP surrogate model.
2. **Surrogate Model Update:** The GP model is trained on the collected data to predict the function's output for unexplored regions of the parameter space. The model provides both mean predictions and uncertainties, allowing BO to assess where to sample next.
3. **Acquisition Function:** The next sample point is selected by optimizing an acquisition function, such as Expected Improvement (EI), which measures the potential value of sampling a given point. This step ensures a good balance between exploration and exploitation.
4. **Iterative Process:** The newly selected point is evaluated, and the surrogate model is updated with the new data. This iterative process continues until a predefined stopping criterion is met (e.g., convergence of the objective function or reaching a set number of iterations).

4.1.1 Why Bayesian Optimization?

Bayesian Optimization is particularly well-suited for this study for several reasons:

- **High Cost of Evaluation:** Each evaluation involves a computationally expensive band structure and topological invariant calculation. BO minimizes the number of required evaluations by strategically choosing where to sample.
- **Uncertainty Quantification:** The GP surrogate provides an uncertainty estimate, which is crucial for exploring the parameter space effectively.
- **Non-convexity and Irregular Objective Landscapes:** The photonic crystal design problem might involve non-convex and complex objective landscapes, which are computationally expensive to calculate fully with multiple local optima. BO's ability to handle such challenges makes it an ideal choice.

4.2 Time Complexity Analysis

The computational cost of Bayesian Optimization is primarily determined by two factors: the cost of training the GP model and the cost of evaluating the acquisition function.

The time complexity for training a GP model scales as $O(N^3)$, where N is the number of observations (evaluations of the objective function). This cubic complexity arises from the inversion of the covariance matrix during training. However, this cost is mitigated by keeping N relatively small through efficient sampling.

The evaluation of the acquisition function involves calculating the expected improvement across the parameter space. This step typically scales linearly with the number of candidate points being considered, which allows for efficient parallelization.

4.3 Figure of Merit

The Figure of Merit (FOM)—named as topological criterion—used in this optimization combines multiple aspects critical for photonic crystal performance:

- **Relative Band Gap:** Defined as the width of the bandgap relative to the central frequency, maximizing this ensures robust mode isolation.
- **Chern Number:** Based on the calculated Chern number that measures the topological robustness of the photonic structure. The goal is to ensure high Chern numbers at the K and K' valleys, indicating strong topological protection.

The topological criterion can be dynamically adapted depending on the specific optimization goal. For example, for devices requiring high topological protection, the weighting of the topological criterion can be increased relative to other components.

4.4 Bayesian Optimization Implementation Details

The implementation of Bayesian Optimization was carried out using the Ax optimization framework in Python. Below, we provide a detailed breakdown of the parameters used in the optimization and their respective roles:

4.4.1 Design Parameters and Ranges

The design parameters optimized in this study include:

- **l_{central} (Central Frequency Parameter):** This parameter decided the central operating frequency of the Valley Photonic Devices that we wish to optimize using this method. There is an approximately linear relation of Central Frequency with l_{central} (ranges between 0 and $\frac{1}{\sqrt{3}}$) as demonstrated in later sections.
- **δ_l (Asymmetry Parameter):** This parameter represents the asymmetry in the circumradius (dimension) of the two air holes in the VPC. The range was set between 0 and $2l_{\text{central}}$, ensuring that the size constraints of the photonic crystal unit cell are respected.
- **symmetry_separation (Symmetry Shift):** This parameter allows for small deviations in the symmetry of the polygonal air holes along the inversion symmetry axis (Longer Diagonal of the Rhombic Unit Cell). It varies between $-0.2a$ and $0.2a$, where a is the lattice constant.
- **rotation_angle (Rotation of Unit Cell):** This parameter controls the rotation of the polygonal air holes with respect to the base position. It is varied between $-\pi/5$ and $\pi/5$ radians, allowing for changes in the orientation of the unit cell, which can influence the band structure and topological properties.

4.4.2 Optimization Process

The Optimization Process detailed below was done for optimizing the Relative Band Gap. The optimization process involved 20 initial evaluations using a Sobol sequence to establish the GP model. Following this, the Expected Improvement acquisition function was used to sequentially identify new points for evaluation, with a total of 50 additional evaluations performed to converge to an optimal solution.

The optimization loop was executed across different values for the polygon side count (3 to 10 sides) along with a circular air hole geometry, allowing us to assess the impact of different unit cell geometries on the figure of merit.

4.5 Results and Analysis

4.5.1 Optimization Results

The optimization results are summarized in Figure 4.1, which shows the convergence of the figure of merit over successive iterations. The figure illustrates that Bayesian Optimization effectively identifies configurations with significantly improved performance metrics compared to the initial designs.

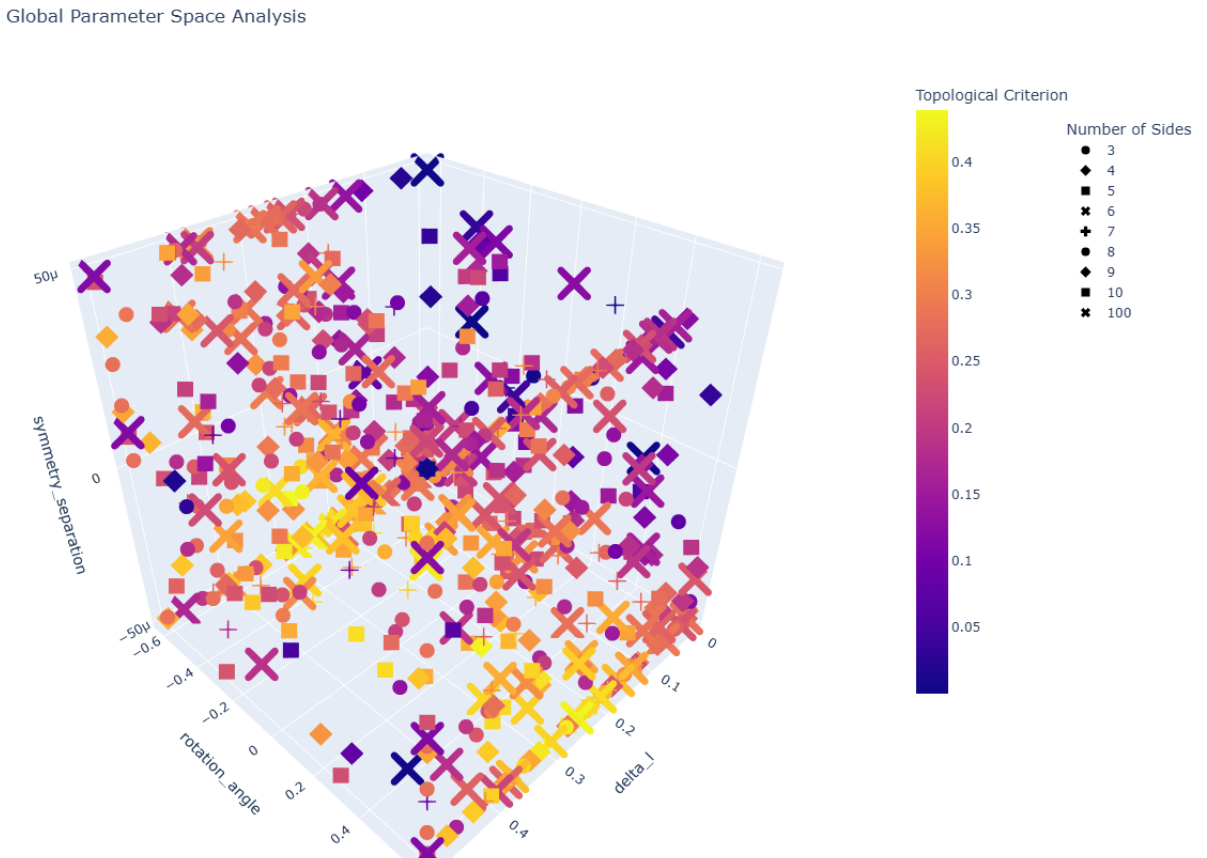


Figure 4.1: Convergence of the Topological Criterion (FOM) (which is the Relative Band Gap here) during Bayesian Optimization. The FOM increases steadily as the optimization progresses, demonstrating the efficacy of Bayesian Optimization. Interactive 3D plot available at [this link](#).

Relative band gap of almost 44% was achieved. Yi Ji Tan., et al. (2022) [14] demonstrated a maximum relative band gap of 42.8% in their paper. The most optimal structure obtained by the optimization can be seen in Figure 4.2.

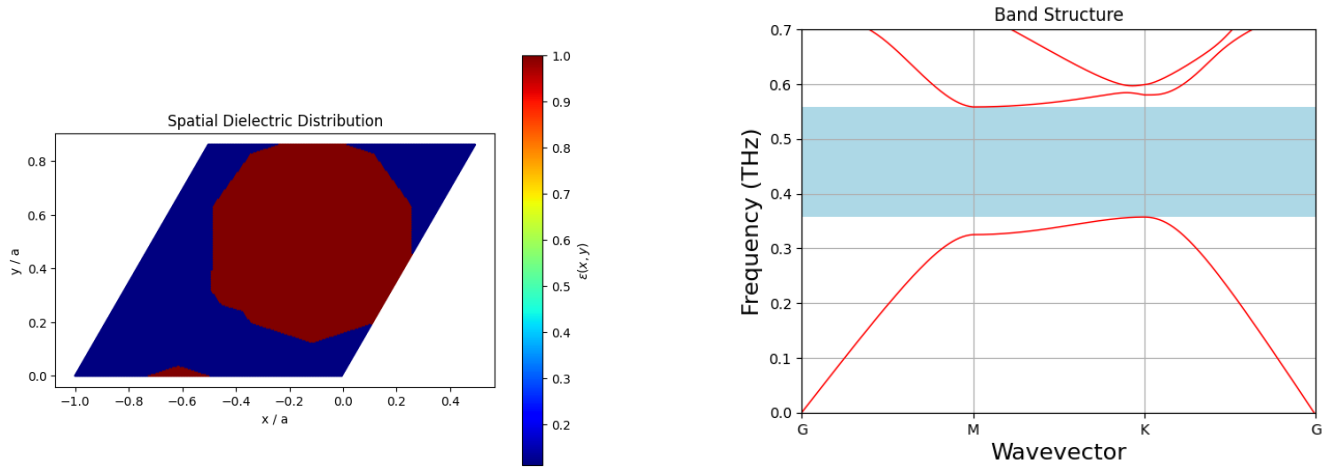


Figure 4.2: Most Optimal Structure from Bayesian Optimization for Maximizing Relative Band Gap. The Parameters are as follows: Number of Sides = 10, $l_{\text{central}} = 0.25$, $\delta_l = 0.281$, symmetry_separation = $-0.130a$, rotation_angle = $\frac{\pi}{5}$

4.5.2 Parameter Analysis and Convergence Study

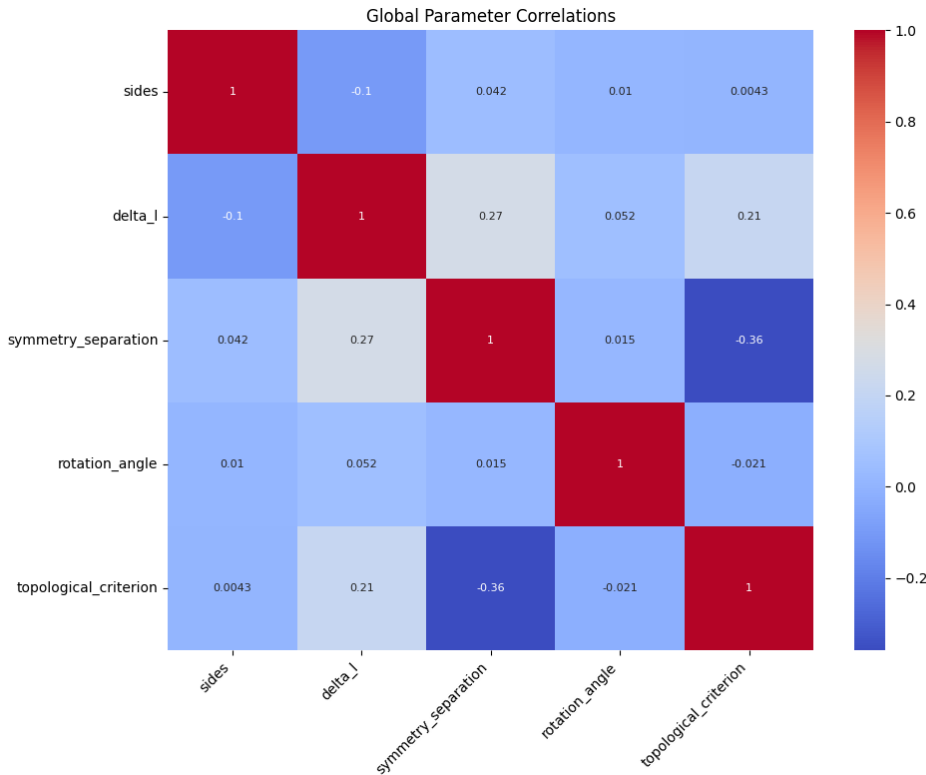


Figure 4.3: Correlation between different parameters and the figure of merit. Understanding these correlations helps in understanding the effect of different parameters.

In addition to optimizing the primary design parameters, we also conducted an analysis of these parameters that govern the Bayesian Optimization process.

To illustrate the relationship between parameters and optimization performance, Figure 4.3 shows the correlations between different parameters and the resulting figure of merit. This analysis helps in identifying the effect that different parameters have on the Topological Criterion (FOM).

In addition to analyzing hyperparameter correlations, we also plotted the convergence of the maximum value of the relative band gap with the number of iterations of the Bayesian Optimization process. This convergence plot (Figure 4.4) is critical to understand how effectively the optimization process identifies an optimal solution over time. The steady rise in the relative band gap indicates the success of the optimization approach in progressively improving the structure's performance.

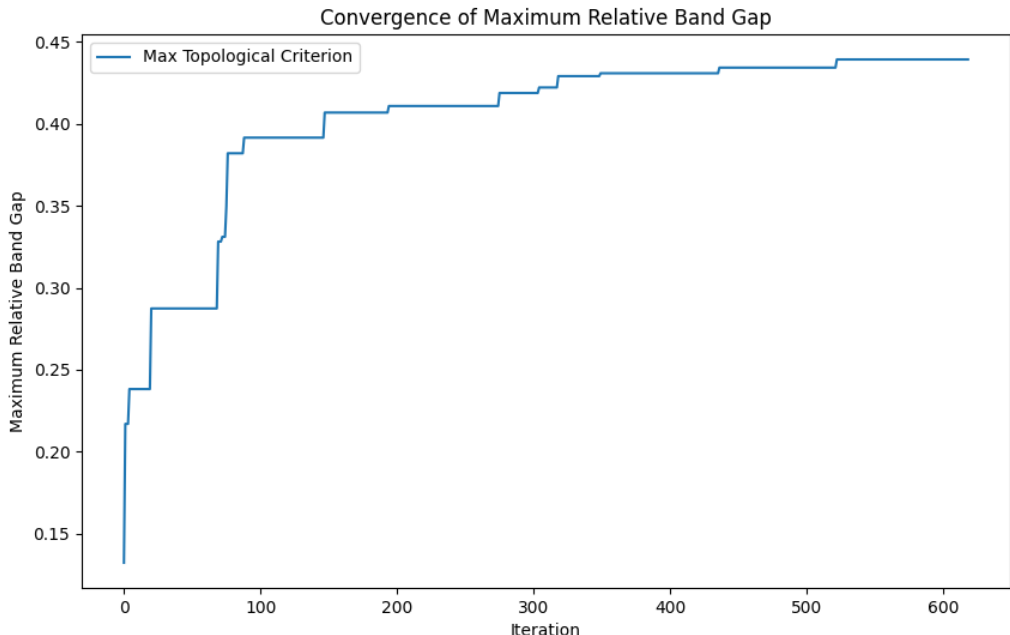


Figure 4.4: Convergence of the maximum value of the relative band gap with the number of iterations.

Summary of Optimization Methodology

The Bayesian Optimization approach adopted in this study successfully identified optimal configurations for the photonic crystal design by balancing accuracy and computational efficiency. The ability to incorporate various objectives into a single figure of merit allowed for the concurrent optimization of band gap and topological protection governed by the Magnitude of the Berry Curvature (or Chern Number).

Chapter 5

Future Work and Conclusion

The optimization work presented in this thesis lays a strong foundation for the design of high-performance photonic crystals. However, there are multiple avenues for further enhancing these designs, as well as opportunities to explore novel physical phenomena and real-world implementation. This chapter outlines the future directions for this research, focusing on alternative optimization methodologies, studies of fabrication imperfections, investigations into the Dirac frequency, and steps towards experimental validation.

5.1 Exploring Alternative Optimization Techniques

While Bayesian Optimization was utilized in this study for its efficiency in handling computationally expensive evaluations and non-convex design spaces, other optimization approaches could provide complementary benefits.

5.1.1 Gradient-free Methods: Particle Swarm Optimization

Particle Swarm Optimization (PSO) is a gradient-free technique inspired by the collective behavior of swarms in nature. It can be highly effective in navigating complex, high-dimensional parameter spaces and finding global optima. PSO could serve as an alternative optimization technique, especially in cases where Bayesian Optimization might struggle with highly irregular objective landscapes. PSO's ability to maintain a diverse population of solutions throughout the optimization process might help in identifying more diverse and robust designs for photonic crystals.

5.1.2 Adjoint Method-Based Shape Optimization

Another promising approach is Adjoint Method-Based Shape Optimization [15], which is particularly useful for achieving fine-tuned designs in photonic structures. The adjoint method enables efficient gradient calculation, allowing for precise control over specific shape parameters. This approach could be used in conjunction with Bayesian Optimization to refine designs that already exhibit desirable topological properties, providing a hybrid optimization strategy to achieve both macroscopic and microscopic improvements.

5.1.3 Moving Towards Neural Network-Based Optimization

Deep learning methods for optimizing Photonic structures[16] [17], particularly Neural Network-based optimization, represent an exciting direction for future work. Neural Networks can be trained to predict the properties of photonic crystals based on input design parameters, significantly reducing the need for computationally expensive simulations. Once trained, these models could facilitate rapid design iteration and optimization. Generative models, such as Variational Autoencoders (VAEs) or Generative Adversarial Networks (GANs), could even be used to generate entirely new photonic crystal geometries with desired properties.

5.2 Detailed Study on Fabrication Imperfections

Fabrication imperfections are inevitable in real-world implementations and can have significant impacts on the performance of photonic crystals. To account for these imperfections, detailed studies using statistical simulations are required. The approach for simulating fabrication imperfections in this study involves adding line-edge roughness, angular deviations, and positional errors to the ideal structure, as detailed in the code used for generating perturbed unit cells.

The imperfections were modeled using several parameters:

- **Line-Edge Roughness (LER):** The roughness amplitude was introduced along the polygon edges to simulate variability during etching or deposition processes.
- **Angular Deviations:** Random variations in the angles between the polygon sides were added to mimic non-idealities in lithographic patterning.

- **Positional Errors:** Small random displacements of the vertices were incorporated to simulate misalignment and fabrication imprecision.
- **Imperfection Length:** This criteria represents the deviation of the air hole dimensions from their ideal dimensions. It is modelled as a Gaussian distribution centered at the ideal values with σ equal to the Imperfection Length parameter.

The goal of this analysis is to quantify the effect of these imperfections on key properties like the band structure, bandgap width, and topological robustness. Figures 5.1 and 5.2 illustrate the distributions of these properties for different levels of imperfections compared with the ideal structure, providing insights into the tolerance limits of the designed structures. Future work will extend this analysis to include advanced statistical models, such as Monte Carlo simulations, to better predict the impact of large-scale variations and potential defect-induced losses.

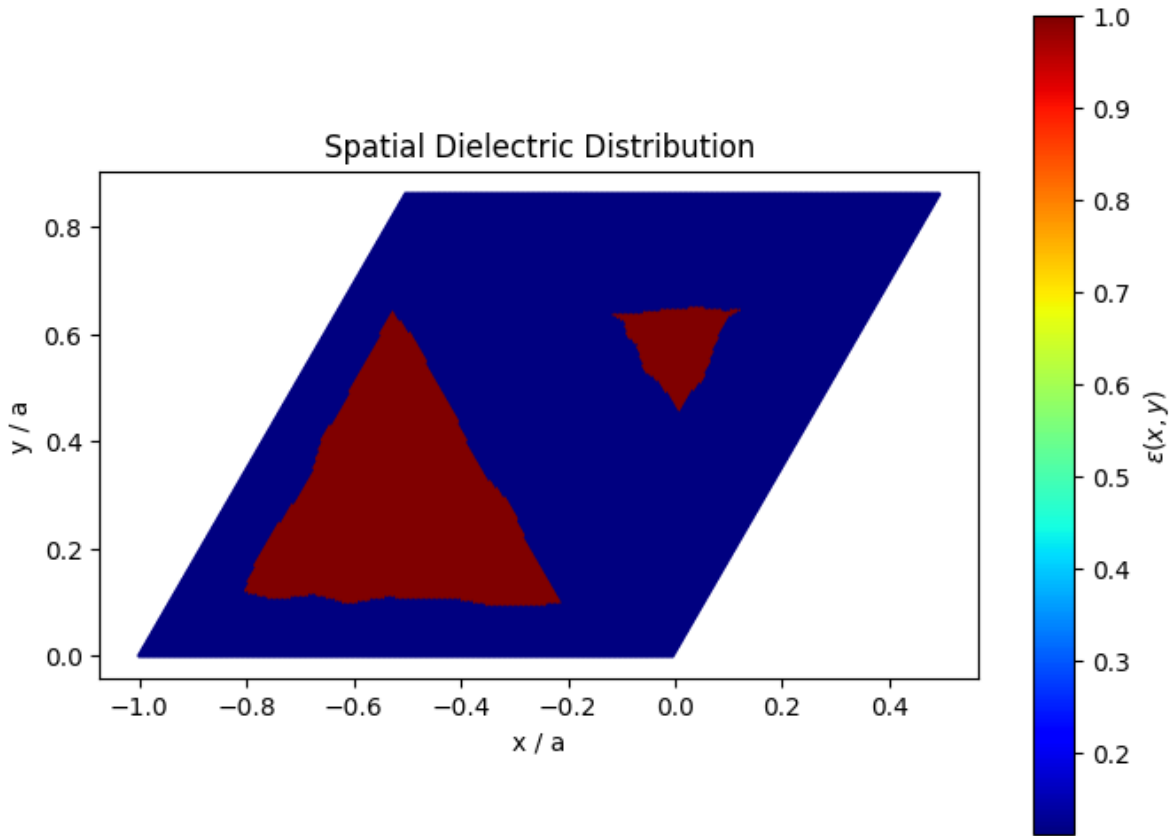


Figure 5.1: Illustration of the photonic crystal structure with fabrication imperfections. Criteria: $l_1 = 0.3520$, $l_2 = 0.1356$. Valley Chern number at $K = 0.1538$, Band Gap = 243.96 GHz

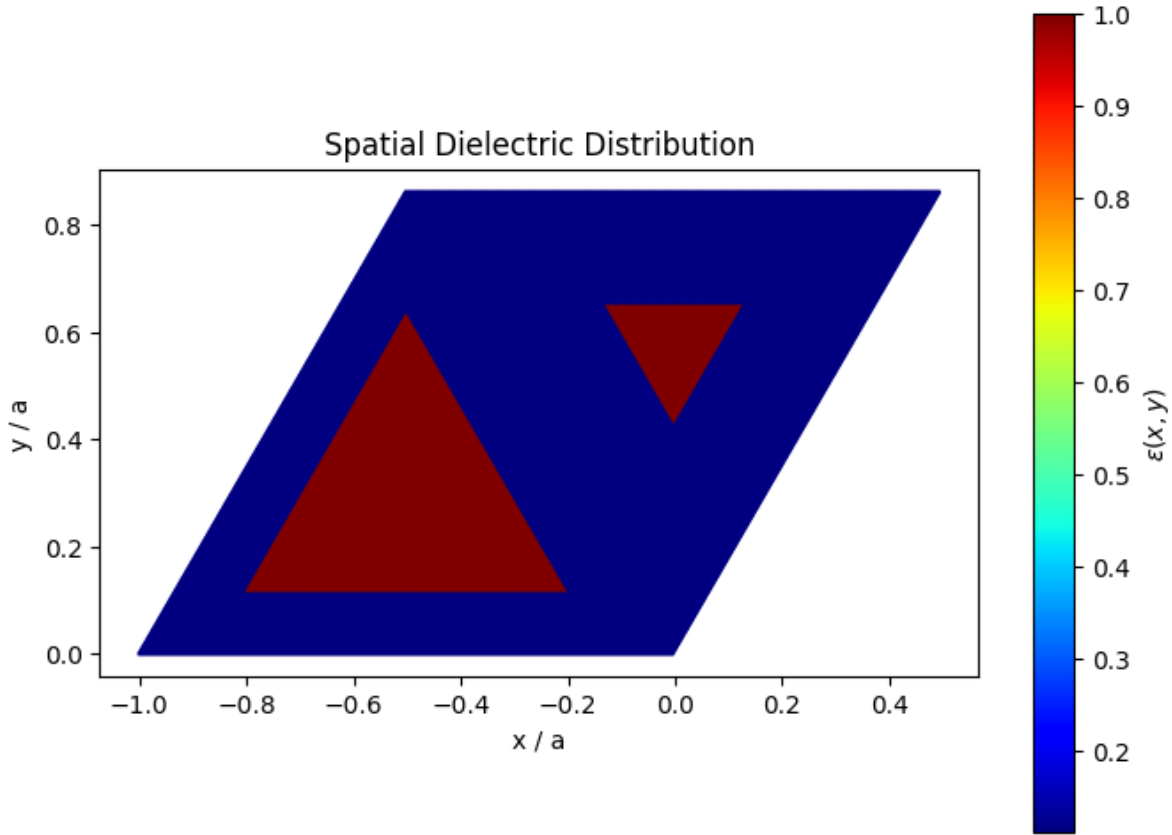


Figure 5.2: Illustration of the ideal photonic crystal structure. Criteria: $l_1 = 0.35$, $l_2 = 0.15$. Chern number at K: 0.1783, Band Gap: 215.84 GHz

5.3 Ongoing Study on Dirac Frequency

Another intriguing direction for future research is the detailed study of the Dirac frequency in photonic crystals. The Dirac frequency is a key point in the band structure where linear dispersions intersect, akin to the Dirac cones observed in electronic systems like graphene. In photonic crystals, the location and properties of this frequency can be influenced by geometric parameters such as the shape and size of the unit cell. Ongoing work aims to determine how slight modifications to these parameters affect the Dirac frequency, with the goal of harnessing new forms of photonic bandgap and transport phenomena. Initial results suggest the presence of novel physical effects, including enhanced light-matter interaction at specific frequencies, which may lead to new applications in sensing and signal processing.

5.4 Pathway to Experimental Validation

The computational results obtained thus far provide a compelling case for experimental validation. The next step will involve fabricating the optimized photonic

crystal structures using high-precision nanofabrication techniques such as electron beam lithography (EBL) and testing them for their intended applications in terahertz (THz) communication systems. Collaborations with experimental groups will be essential for verifying the predicted properties, including bandgap formation, robustness against defects, and efficient waveguiding through topologically protected edge states. The successful transition from simulation to experimental verification will pave the way for practical, on-chip photonic devices.

5.5 Conclusion

In conclusion, this thesis presents a comprehensive study of photonic crystal optimization, leveraging Bayesian Optimization to systematically improve their performance for terahertz communication and integrated photonic circuits. The results demonstrate significant enhancements in key properties, including bandgap width, topological robustness, and defect tolerance. However, much work remains to be done. Future studies will focus on incorporating other optimization methods, accounting for real-world fabrication imperfections, and validating the designs experimentally. The promising initial results for the Dirac frequency also indicate the potential for uncovering novel photonic phenomena that could further broaden the application scope of these devices. Overall, this research contributes to the ongoing efforts to harness the unique properties of photonic crystals for next-generation communication and sensing technologies.

BTP 2 - Spring Semester (2024–25)

Chapters 6 to 7 of this thesis were completed in the Spring Semester (2024-25) as part of the work done in PH 588 - B.Tech. Project 2.

Abstract

In the second phase of the thesis, we expanded upon the initial Bayesian optimization framework by incorporating a custom Mixed-Integer Particle Swarm Optimization (PSO) algorithm tailored for discrete and continuous design variables of Valley Photonic Crystals. The PSO approach enabled deeper exploration of the 6-dimensional parameter space, leading to a significantly enhanced topological figure of merit. Chapter 6 details this optimization framework, including algorithmic modifications, parameter update strategies, and parallel coordinate/correlation analyses of the design space.

Furthermore, Chapter 7 discusses the implementation of domain wall transport simulations in COMSOL Multiphysics using the optimized photonic crystal structure. Waveguide geometries were constructed to validate robust, defect-tolerant propagation of topologically protected edge states. The COMSOL simulations confirmed localized transport and zero backscattering, reinforcing the practical applicability of the optimized designs for integrated THz photonic circuits.

Chapter 6

Modified PSO Optimization Methodology

In the previous chapters, we established the theoretical foundations of valley photonic crystals (VPCs) and analyzed a baseline design with a modest topological band gap. We now focus on systematically improving the VPC design using a computational optimization approach. This chapter presents a **modified particle swarm optimization (PSO)** methodology tailored for the mixed continuous-discrete parameter space of the VPC unit cell. The goal is to maximize a topological figure-of-merit combining the relative band gap size and the valley Chern number, thereby identifying geometries with large topological band gaps for robust 6G communication links. We describe the formulation of the mixed-integer PSO algorithm, including the incorporation of discrete geometry parameters (polygon side counts) and continuous parameters (feature sizes and rotations). We also detail the **sequential simulation pipeline** – from unit cell construction through band structure calculation and Berry curvature integration – which evaluates the objective for each candidate design. Finally, we present the optimization results, including the converged design parameters, the achieved band gap and Chern number, and discuss the improvements over the baseline design (Chapter 3). Figure 6.1 provides a schematic overview of the optimization workflow employed in this chapter.

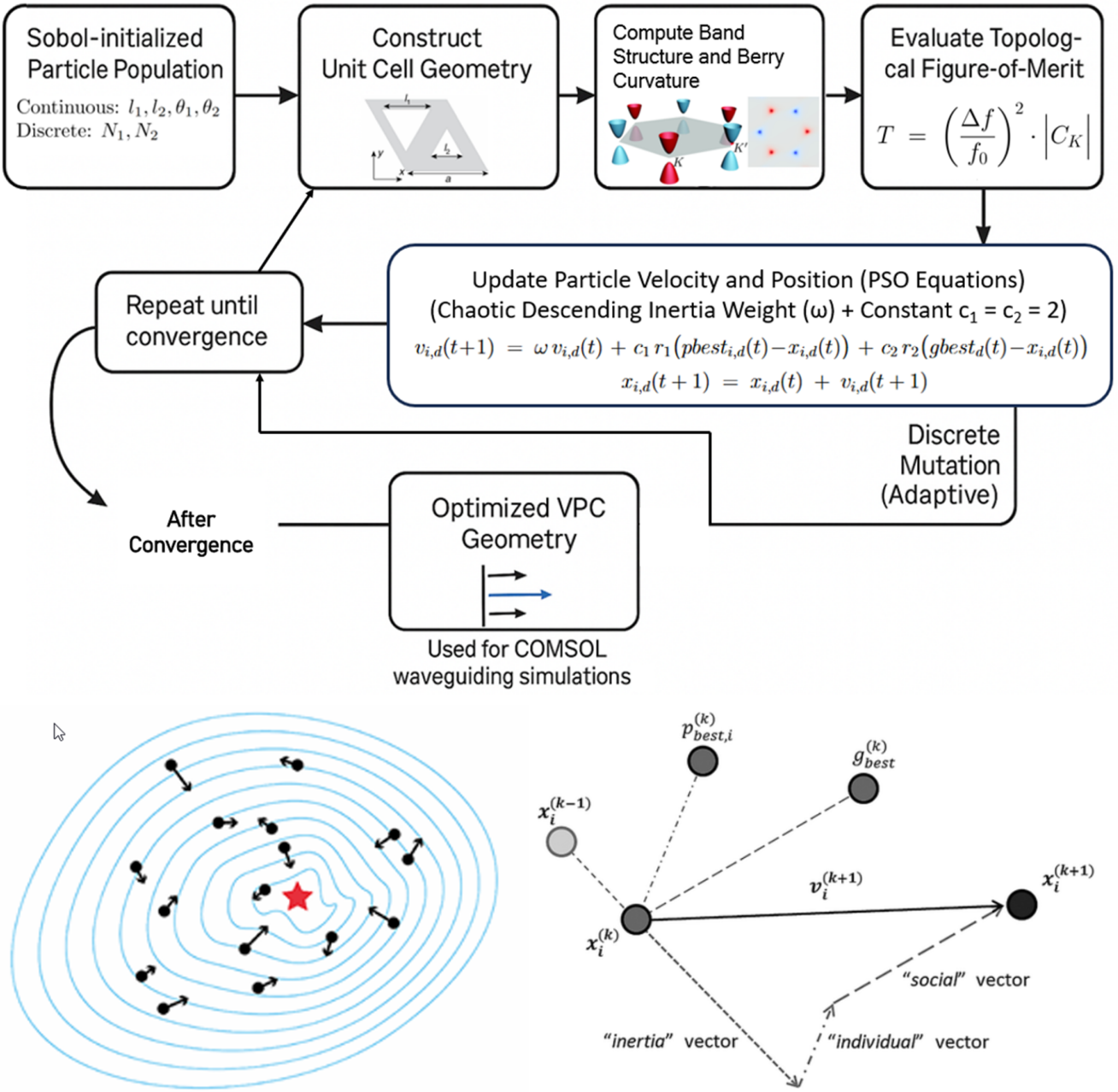


Figure 6.1: (Top) Schematic of the PSO-based optimization workflow for VPC design. The process begins with Sobol-initialized particle positions in the 6D design space. Each iteration involves constructing a unit cell from particle parameters, computing its band diagram and topological properties, and evaluating the figure-of-merit. Particle positions (designs) are then updated using PSO velocity equations and a mutation operator for discrete variables. The loop repeats until convergence criteria are met.

(Bottom Left) Schematic for a General Particle Swarm Optimization Scheme.

(Bottom Right) Velocity and Position Update Scheme for Particle Swarm Optimization.

6.1 Mixed-Integer Particle Swarm Optimization Algorithm

Particle swarm optimization is a population-based, stochastic optimization algorithm inspired by social behaviors in flocks of birds or schools of fish. In PSO, a set of candidate solutions (called particles) “fly” through the search space, adjusting their position based on both their own experience and shared information from the swarm. In our application, each particle represents a specific photonic crystal unit cell design defined by a set of parameters. Standard PSO operates in a continuous search space; however, our design space includes mixed-integer variables – specifically, two discrete variables defining polygon shapes. We therefore implement a modified PSO that can handle both continuous and discrete parameters. The swarm’s task is to optimize a 6-dimensional parameter vector $\mathbf{x} = [l_1, l_2, \theta_1, \theta_2, N_1, N_2]$, where l_1 and l_2 are continuous length parameters, θ_1 and θ_2 are continuous rotation angles, and N_1, N_2 are discrete number of sides for the two polygonal holes in the unit cell. The incorporation of N_1 and N_2 (with allowable integer values from 3 up to 360, where $N = 360$ effectively represents a circular shape) makes this a mixed-integer optimization problem.

6.1.1 Design Variables and Parameterization

Each particle’s position encodes a unique unit cell geometry in the VPC. The two continuous length parameters l_1 and l_2 control the size (e.g., radius or side length) of the two polygonal apertures (or dielectric inclusions) located at the two inequivalent lattice sites of the hexagonal unit cell. These values are normalized relative to the lattice constant a to ensure a consistent scale – for example, we define l_1 and l_2 as fractions of the maximum inscribed radius within the unit cell. In this work, we bound $l_1, l_2 \in [0.05a/\sqrt{3}, 0.95a/\sqrt{3}]$, which (for lattice constant $a = 242.5\text{ }\mu\text{m}$) corresponds roughly to $[0.02a, 0.55a]$. This range prevents the polygons from becoming too small (avoiding numerical issues and negligible perturbation) or too large (avoiding overlap between neighboring unit cells).

The discrete variables N_1 and N_2 determine the shape geometry of the two holes: a value of $N = 3$ corresponds to a triangular hole, $N = 4$ a square, $N = 6$ a hexagon, and so on, up to $N = 360$ which is treated as a near-circular hole. By allowing a wide range of N , the optimizer can explore a continuum from highly faceted polygons

to virtually circular shapes. The rotation angles θ_1 and θ_2 (continuous) specify the orientation of each polygon relative to a reference orientation (e.g., alignment to the lattice vectors). Rotating the shapes differently on the two sublattices is a key mechanism for breaking inversion symmetry and inducing a valley-dependent band gap (as discussed in Chapter 2). Due to the N -fold rotational symmetry of a regular N -sided polygon, a rotation by $2\pi/N$ returns the shape to an equivalent orientation. Therefore, we impose a normalization on θ_1 and θ_2 such that each angle is effectively constrained to the range $[-\pi/N_i, +\pi/N_i]$ for its current polygon N_i . In practice, during the optimization we track the *normalized rotation* $\bar{\theta}_i = \theta_i \cdot N_i/\pi$, which lies in $[-1, +1]$. This ensures that the optimizer does not waste exploration on redundant rotations beyond the fundamental symmetric range. If a particle changes its N_i value (shape sides), the corresponding θ_i is reinterpreted with respect to the new symmetry. This strategy effectively handles rotational degrees of freedom in a discontinuous shape space.

6.1.2 Swarm Initialization and Update Equations

We initialize the swarm of P particles using a Sobol quasi-random sequence [18] to sample the 6D design space. Unlike purely random initialization, the Sobol sequence provides a low-discrepancy distribution of initial particle positions, which improves coverage of the search space and prevents clustering of initial solutions (See Figure 6.1). Each particle is assigned random l_1, l_2 within the allowed range, random θ_1, θ_2 within $[-\pi/N_i, \pi/N_i]$ (with an initial guess for N_i when computing this range), and random integer choices for N_1, N_2 selected uniformly from the allowed set $\{3, 4, 5, 6, 7, 8, 9, 12, 360\}$ (here we limit to a representative subset including 12 and then 360 for near-circle, to reduce search complexity). The initial swarm thus contains a diverse mix of geometries (triangles, squares, pentagons, etc., in various orientations and sizes).

At each iteration t of the PSO, every particle i has an associated velocity vector $\mathbf{v}_i(t)$ in the same 6-dimensional space as the position $\mathbf{x}_i(t)$. The algorithm updates these velocities and positions according to the standard PSO rules, modified to accommodate our variables. For the continuous dimensions $(l_1, l_2, \theta_1, \theta_2)$, we use the conventional PSO update equations. Specifically, for each continuous dimension d of particle i :

$$v_{i,d}(t+1) = \omega v_{i,d}(t) + c_1 r_1(pbest_{i,d}(t) - x_{i,d}(t)) + c_2 r_2(gbest_d(t) - x_{i,d}(t)) \quad (6.1)$$

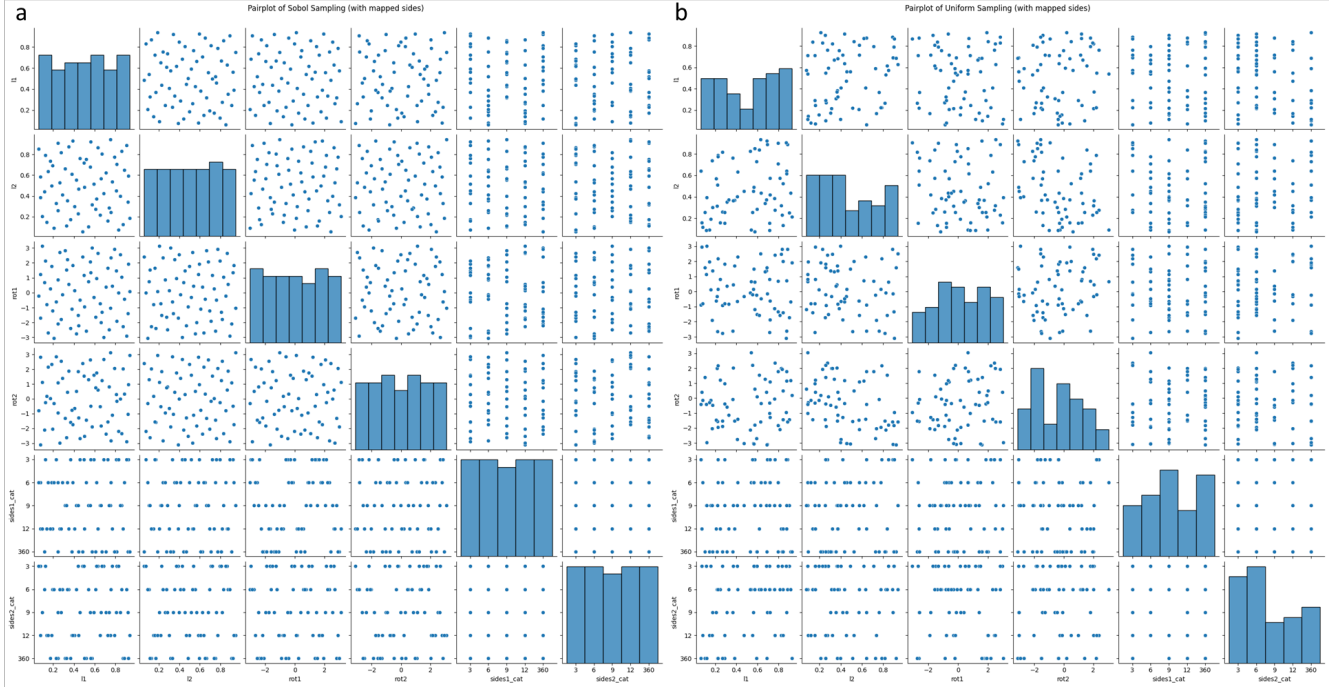


Figure 6.2: Comparison of parameter space coverage using (a) Sobol Sampling and (b) Uniform Sampling for initializing the particle population in a 6D mixed-variable space for Particle Swarm Optimization (PSO). The continuous dimensions include l_1 , l_2 , θ_1 , and θ_2 (mapped to `rot1` and `rot2`), while the categorical variables N_1 and N_2 (polygon side counts) are mapped to `sides1_cat` and `sides2_cat`. The Sobol sampling strategy (left) provides a more uniform and stratified coverage of the parameter space compared to the irregular clustering observed in uniform random sampling (right), thereby facilitating improved exploration and convergence in high-dimensional optimization.

$$x_{i,d}(t+1) = x_{i,d}(t) + v_{i,d}(t+1) \quad (6.2)$$

where ω is the inertia weight balancing exploration and exploitation, c_1 and c_2 are the cognitive and social acceleration coefficients respectively, r_1 and r_2 are independent random numbers in $[0, 1]$, $pbest_i$ is the best position found so far by particle i , and $gbest$ is the best position found by the entire swarm up to the current iteration.

6.1.3 PSO Parameter Update Strategies

In our implementation of the Mixed-Integer Particle Swarm Optimization (PSO), we adopt parameter settings confirmed by empirical studies to yield robust convergence. Specifically, we set the cognitive and social coefficients to constant values $c_1 = c_2 = 2.0$, as supported by several benchmark studies in the PSO literature [19] [20]. For

the inertia weight ω , we employ a *chaotic descending inertia strategy* [21]: at each iteration, ω is dynamically adapted using a logistic chaotic map modulated by a linearly decaying envelope. This approach encourages global exploration in early iterations and enables fine-grained local search in later stages, enhancing convergence to high-quality solutions. This approach is shown to give the best results for Particle Swarm Optimization in terms of Average Error out of several different inertia weight strategies [22]. The chaotic descending inertia strategy implementation follows:

$$z = 4 \times z \times (1 - z)$$

$$w = (w_1 - w_2) \times \frac{\text{MAXiter} - \text{iter}}{\text{MAXiter}} + w_2 \times z$$

The optimization problem spans a 6D mixed-variable space comprising four continuous variables ($l_1, l_2, \theta_1, \theta_2$) and two discrete variables (N_1, N_2), corresponding to geometric and symmetry parameters of the photonic unit cell.

Continuous Variable Updates

Continuous parameters are updated using the canonical PSO update rule:

$$\vec{v}_i^{(t+1)} = \omega \vec{v}_i^{(t)} + c_1 \vec{r}_1 \odot (\vec{p}_i^{\text{best}} - \vec{x}_i^{(t)}) + c_2 \vec{r}_2 \odot (\vec{g}^{\text{best}} - \vec{x}_i^{(t)}), \quad (6.3)$$

$$\vec{x}_i^{(t+1)} = \vec{x}_i^{(t)} + \vec{v}_i^{(t+1)}, \quad (6.4)$$

where \vec{x}_i and \vec{v}_i are the position and velocity of the i th particle, respectively, and $\vec{p}_i^{\text{best}}, \vec{g}^{\text{best}}$ are the personal and global best positions. After each update, the continuous variables are clamped to their respective bounds. Rotation angles θ_1, θ_2 are normalized and restricted to their symmetric ranges $[-\pi/N, +\pi/N]$ for each polygonal symmetry N .

Discrete Variable Updates

Standard PSO updates do not extend naturally to discrete (categorical) variables like the polygon side counts N_1, N_2 . Hence, we introduce a custom *probabilistic discrete update operator* after each continuous update. For each particle, and for each discrete variable, we probabilistically choose one of three update strategies:

- **Mutation:** With a probability P_{mut} , the discrete variable is reassigned to a random new value from the allowed set $\{3, 4, 5, 6, 7, 8, 9, 12, 360\}$, excluding the current value.

- **Migration:** With probability P_{mig} , the particle copies the corresponding discrete variable from the current global best, effectively “migrating” towards high-performing discrete configurations.
- **Preservation:** With the remaining probability $1 - P_{\text{mut}} - P_{\text{mig}}$, the particle retains its existing value, enabling local refinement.

This tri-modal update mechanism allows particles to *explore new topological configurations, inherit globally beneficial designs, or refine their current configurations*, thus balancing diversity and convergence.

To maintain dynamism, the **mutation probability** P_{mut} is sampled randomly at each iteration from a bounded range (e.g., 0.15 to 0.25), encouraging stochastic exploration without deterministic decay. A small **migration probability** (e.g., 0.10) complements this by providing a controlled attractor towards the global optimum. Together, these probabilities control the “jump” between discrete symmetry subspaces (e.g., from triangular to circular holes), enabling rich, multi-modal search behavior across the hybrid design space.

Upon mutation or migration of a discrete variable, the corresponding rotation angle θ_i is re-initialized or re-normalized to ensure compatibility with the new polygonal symmetry.

This hybrid discrete-continuous update scheme is essential for the *topology-aware optimization of Valley Photonic Crystals*, where both geometry and symmetry crucially affect topological band gaps and Berry curvature distribution.

The overall PSO algorithm alternates between objective evaluation (see Section 4.2) and swarm update (using Eqs. 6.1–6.2 and the mutation rule). The process is iterated for a fixed number of iterations T or until convergence criteria are met (e.g., if improvements fall below a threshold). In our case, we ran the optimization for $T = 50$ iterations with a swarm size $P = 20$, which was sufficient for the objective to converge. Figure 6.3 illustrates the evolution of the swarm in the design space over iterations, projected onto select dimensions. The swarm initially scatters across various design configurations, then gradually clusters as particles discover regions of high performance, finally converging near the optimum design.

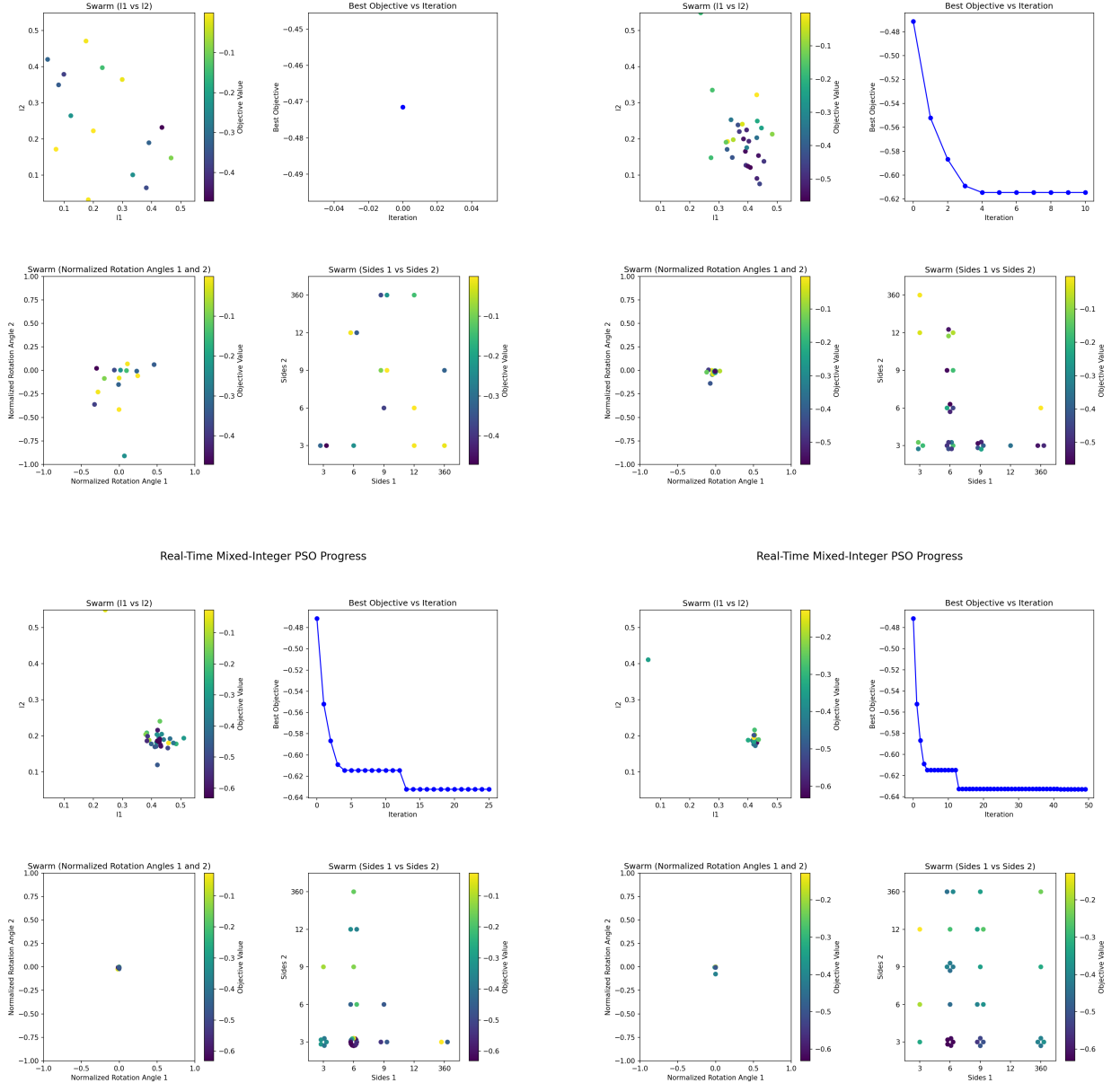


Figure 6.3: Evolution of particle positions in the Mixed-Integer Particle Swarm Optimization (PSO) at different stages of the optimization: (Top Left) iteration 1, (Top Right) iteration 10, (Bottom Left) iteration 25, and (Bottom Right) iteration 50. Each panel displays 2D projections of the 6D swarm population colored by objective value. Top-left: distribution of particles in the continuous design space (l_1 vs. l_2), Top-right: best objective value as a function of iteration. Bottom-left: normalized rotations θ_1 vs. θ_2 , and Bottom-right: discrete categorical variables N_1 vs. N_2 representing polygon side counts. As iterations proceed, the swarm evolves from a dispersed initial configuration to a localized cluster in parameter space near the optimal solution.

6.2 Topological Objective Function and Evaluation Pipeline

Evaluating the fitness (objective value) of each particle’s design requires a multi-step simulation pipeline that computes the photonic band structure and topological properties of the proposed unit cell. This section describes the sequential unit cell simulation workflow and defines the topological figure-of-merit that the PSO maximizes. The sequence for evaluating a given particle’s parameters $\{l_1, l_2, \theta_1, \theta_2, N_1, N_2\}$ is as follows:

Figure ?? shows an example of a unit cell geometry defined by one of the candidate designs (placeholder).

2. Band Structure Computation (PWE): We then solve for the photonic band structure of the unit cell using the Plane Wave Expansion (PWE) method (see Chapter 3 for the PWE formulation). The PWE code calculates the eigenfrequencies $\omega_n(\mathbf{k})$ for Bloch waves in the periodic structure, typically along high-symmetry directions in the Brillouin zone. Of particular interest is the frequency gap opening at the K (and K') valley points of the Brillouin zone. For each design, we extract the fundamental band gap Δf (if any) that opens between the first two photonic bands. Specifically, we look at the frequencies of the first and second bands at the K point: if a band gap exists, the second band’s minimum is above the first band’s maximum, and the difference gives the band gap. We compute the **relative band gap** $\Delta f/f_0$, where f_0 is the mid-gap frequency (or equivalently we can use the Dirac point frequency from the unperturbed lattice as a reference). This normalization is important for comparing gaps at different frequency scales. If no gap opens (bands remain degenerate), the relative gap is 0 and the objective will be poor.

3. Berry Curvature and Chern Number: For designs that exhibit a band gap, we proceed to evaluate their topological character by computing the Berry curvature of the relevant bands. Using the eigenmodes from the PWE solution, we calculate the Berry curvature $F(\mathbf{k})$ for the valence band (the band below the gap) over the Brillouin zone (BZ), following the approach described in Chapter 2.7. We focus on the distribution of $F(\mathbf{k})$ in the vicinity of the K and K' points. Since the structure breaks inversion but preserves time-reversal symmetry, the total Chern number of all bands remains zero, but a **valley-specific Chern number** can be defined by integrating the Berry curvature over half of the Brillouin zone

(enclosing one valley). We integrate $F(\mathbf{k})$ over the K valley region (for example, within the red triangular region surrounding the K point in the BZ) to obtain the valley Chern number C_K . Similarly, integration around K' yields $C_{K'}$, which in theory should satisfy $C_K = -C_{K'}$ for time-reversed pairs. In practice, due to numerical sampling, we compute both and take the average magnitude as the valley Chern number magnitude $|C_K|$. For a strongly topological valley phase, one expects $C_K = \pm 1/2$ or ± 1 for the single-valley integration (some literature defines it as half-integer per valley, but here we normalize it to an integer by integrating over a half-zone). Our computation yields a C_K typically around ± 1 for successful designs, whereas if inversion symmetry is only weakly broken, C_K might be a smaller fraction or the Berry curvature is not well localized (indicating an almost trivial phase).

4. Topological Figure-of-Merit: Finally, we compute the objective function (fitness) for the PSO as a single scalar value. We define the topological figure-of-merit T as

$$T = \left(\frac{\Delta f}{f_0} \right)^2 \cdot |C_K|, \quad (6.5)$$

which is the square of the relative band gap multiplied by the absolute valley Chern number. The squaring of the relative gap heavily incentivizes larger band gaps (a gap twice as large improves the score by a factor of four, all else equal), while multiplying by $|C_K|$ ensures that only topologically nontrivial gaps (those with nonzero Chern number) yield a high score. Designs that do not open a gap or have $C_K \approx 0$ receive $T \approx 0$ and are thus disfavored. In practice, we scale T by a constant factor (e.g., 100) for numerical convenience, but this does not affect the optimization outcome. The PSO uses T as the objective to maximize. After computing T for a particle's design, that value is fed back into the PSO algorithm to update the particle's personal best ($pbest$) and possibly the global best ($gbest$). The next iteration then proceeds with the swarm update as described earlier.

This entire evaluation pipeline is repeated for each particle at each iteration — a procedure that is computationally intensive but embarrassingly parallel (though in our implementation we ran it sequentially for simplicity). The sequential nature of the evaluations means the algorithm evaluates one design fully (steps 1–4) before moving to the next particle; however, since each particle's evaluation is independent, parallel computing could be leveraged to speed up the process in future work.

6.3 Optimization Results and Discussion

6.3.1 Visualization and Analysis of Optimization Landscape

To better understand the geometry of the optimization landscape explored by the modified PSO algorithm, we analyze the distribution and mutual relationships of all six design parameters (two polygonal side counts, two side length ratios, and two normalized rotation angles), alongside the computed topological figure-of-merit (FOM).

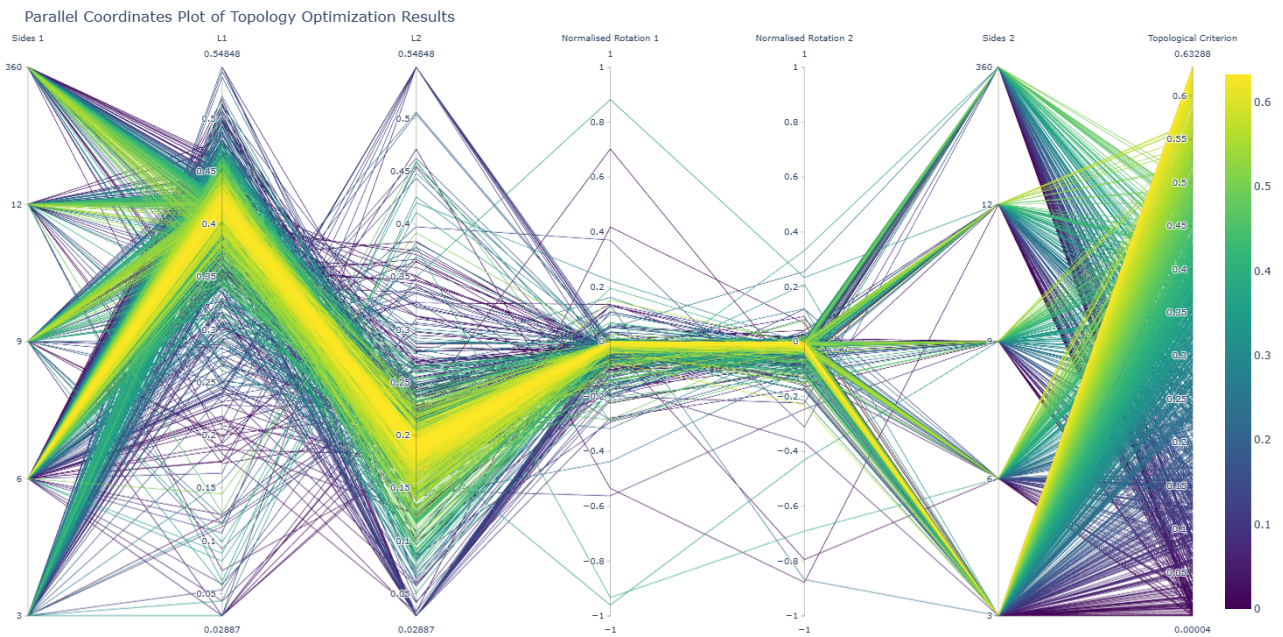


Figure 6.4: Parallel coordinates plot of the PSO optimization results. Each line represents one particle evaluation in the 6D design space, colored by the final value of the topological figure-of-merit: $T = \left(\frac{\Delta f}{f_0}\right)^2 \cdot |\mathcal{C}_K|$. Clear structural patterns emerge for certain discrete configurations (e.g., sides = 6, 9), and optimal designs cluster around intermediate values of L_1, L_2 .

Figure 6.4 shows a parallel coordinates plot of all sampled structures during the PSO run. The FOM color gradient reveals correlations between certain geometric parameters and topological performance. Notably, the best-performing designs typically cluster around moderate length ratios and nearly zero rotation angles.

Figure 6.5 quantifies the linear dependencies between the design variables and the figure-of-merit using Pearson correlation coefficients. As expected, the discrete variables (`sides_1`, `sides_2`) show weak correlation due to their non-continuous nature, while certain combinations of continuous variables (L_1, L_2) and their principal com-

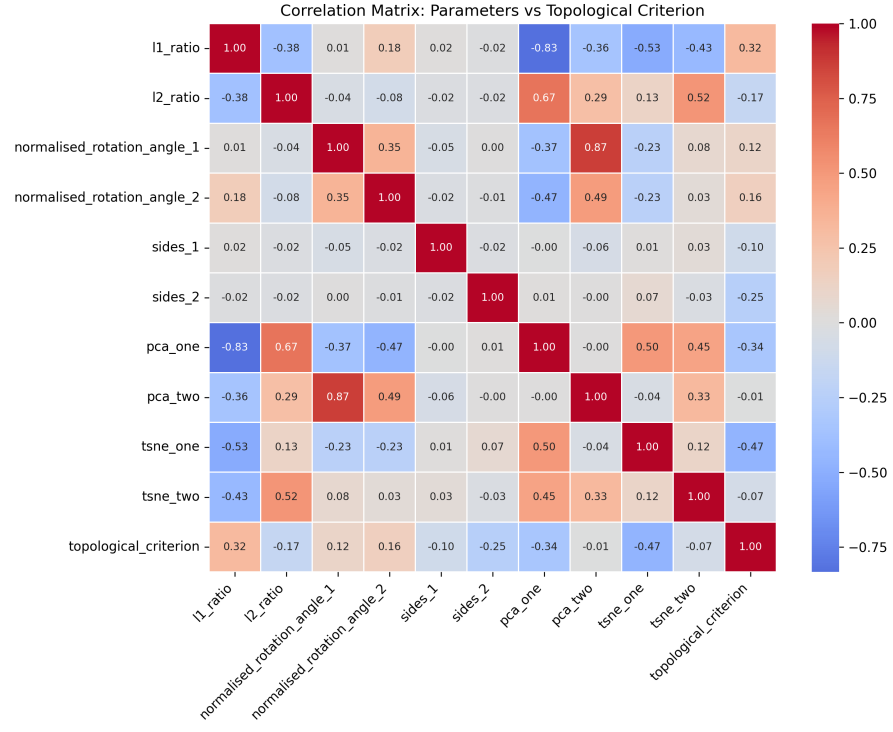


Figure 6.5: Pearson correlation matrix between geometric parameters and topological criterion, including principal components (PCA) and t-SNE coordinates. Strong correlations (both positive and negative) are visible between some features and the FOM, offering insights into design sensitivities.

ponents display moderate to strong correlations with performance. This justifies the use of dimensionality-reduced features for intuitive exploration.

Figures 6.6 show the dimensionality-reduced embedding of the full PSO trajectory using t-distributed Stochastic Neighbor Embedding (t-SNE) (**left**) and Principal Component Analysis (PCA) (**right**), respectively. The FOM-based color encoding reveals that high-performing designs lie on tightly clustered manifolds within the space, further confirming the effectiveness of the PSO algorithm in navigating toward optima despite the presence of mixed-integer design variables.

These visualizations offer post hoc interpretability of the search space structure, guiding future sampling strategies and hybrid exploration methods (e.g., PSO + GP-based surrogate refinement).

After running the PSO optimization with the methodology above, the algorithm converged on a set of optimized parameters that maximize the topological figure-of-merit. Figure 6.7 shows the progression of the global best objective value T over the course of the optimization. We see that T rises rapidly in the early iterations as the swarm discovers designs that open a band gap, and then more gradually as it fine-

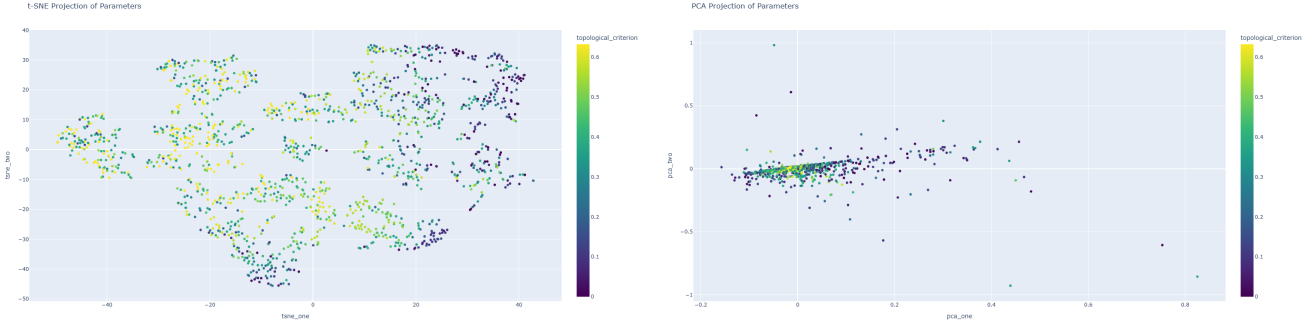


Figure 6.6: t-SNE projection of the 6D parameter space. Each point corresponds to a VPC design evaluated during PSO, colored by topological figure-of-merit. Clusters of high-performance regions are observed, validating convergence toward locally optimal designs. PCA projection of the 6D design parameters, with color map representing the topological figure-of-merit. Unlike t-SNE, PCA offers linear interpretability, highlighting narrow optimal regions in the design space.

tunes the gap size and Chern number. Convergence is reached by around iteration 40, after which T saturates, indicating that further iterations yield no significant improvement. The best-performing design identified by the PSO has the parameters summarized in Table 6.1. Notably, the optimizer chose two very different shapes for the two sublattice holes: one shape with $N_1 = 8$ sides (octagonal-like) and the other with $N_2 = 360$ (effectively circular). The size parameters l_1 and l_2 are also distinct, meaning the two holes differ in both shape and scale. The optimal rotation angles θ_1 and θ_2 are relatively small (on the order of a few degrees), indicating that neither shape is aligned exactly with the lattice axes – a slight rotation likely further breaks symmetry and maximizes the gap. This result is intriguing because earlier studies (and our baseline design in Chapter 3) often used identical shapes (e.g., both triangles) with one rotated relative to the other to break inversion symmetry. Here, the algorithm found that using non-identical shapes yields an even larger band gap. Intuitively, using drastically different shapes (one nearly circular, one polygonal) breaks the sublattice symmetry more strongly, which opens a larger gap, while the small rotations fine-tune the Berry curvature distribution to ensure a high $|C_K|$. From Table 6.1, we see that the optimized design achieves a relative band gap of approximately 29%, centered around $f_0 \approx 0.48$ THz. This is a substantial improvement compared to the baseline triangular-hole design analyzed in Chapter 3, which had a smaller gap (on the order of 5–10%). The valley Chern number magnitude is $|C_K| = 0.077$, indicating a clearly nontrivial topological phase (in contrast, a triv-

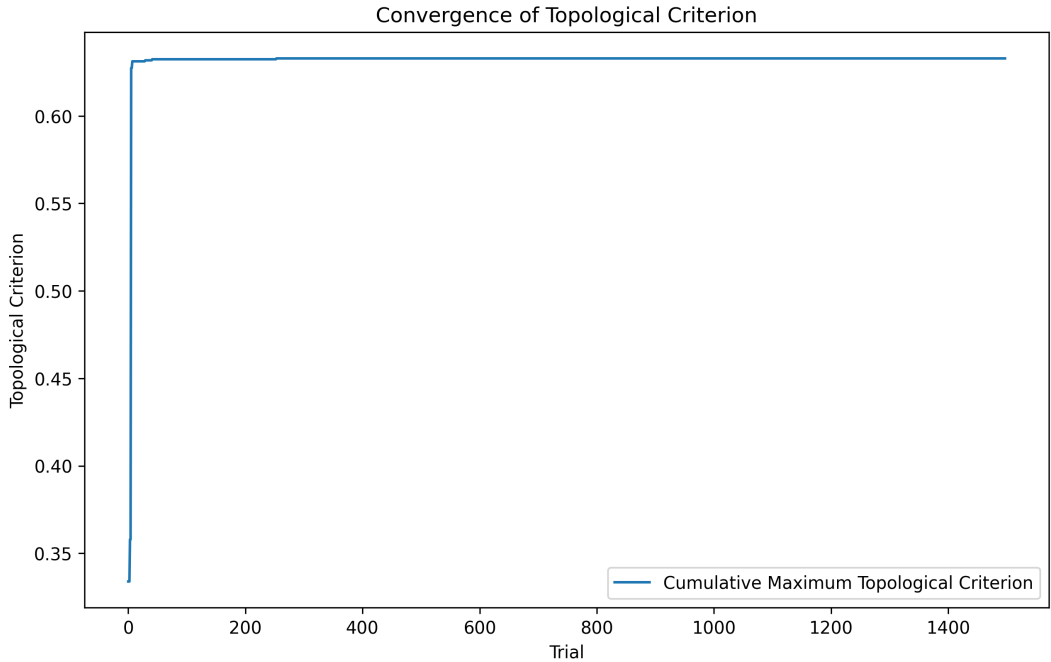


Figure 6.7: PSO convergence curve. The global best objective T is plotted versus iteration number. The rapid initial increase corresponds to the swarm finding designs that open a nonzero band gap. The slower later improvements reflect incremental increases in gap size and optimization of the Berry curvature. By iteration ~ 40 the curve flattens, indicating convergence to the optimum.

Table 6.1: Optimized VPC unit cell parameters and performance metrics. (Note: l_1, l_2 are given as fractions of the lattice constant a , θ_1, θ_2 are in degrees, N_1, N_2 are the number of polygon sides. f_0 is the mid-gap frequency.)

Parameter	l_1	l_2	θ_1	θ_2	N_1	N_2
Optimized values	0.4212	0.1872	0°	0°	6	3
Performance Outcome						
Relative band gap $\Delta f/f_0$	0.29 (29%)		Mid-gap $f_0 = 0.48$ THz			
Valley Chern number C_K			+0.077 (with $C_{K'} = -0.077$)			
Topological FOM T			$0.29^2 \times 0.077 \times 100 = 0.65$ (arbitrary units)			

ial design would have $C_K \approx 0$). The combination of a large gap and C_K yields a high figure-of-merit T . Figures 6.8 correspond to this optimized set of parameters, confirming the presence of the large gap and the concentration of Berry curvature at the valleys. We note that while $N_2 = 360$ (circular hole) has no intrinsic orientation, the other shape $N_1 = 8$ being rotated by about 5° relative to the lattice likely maximizes asymmetry. If both shapes were circles ($N_1 = N_2 = 360$), inversion

symmetry would not be broken and C_K would drop to zero; if both were identical octagons with zero relative rotation, the symmetry breaking would be weaker and the gap smaller. Thus, the optimizer effectively found a sweet spot: using a highly symmetric shape on one sublattice and a less symmetric shape on the other, plus a slight rotational misalignment, to maximize the valley Hall effect.

To visualize the optimized unit cell’s effect on wave propagation, one would create a domain wall (interface) between two regions of this crystal with opposite “valley configurations” (for example, by interchanging the two shapes between sublattices in the adjacent domain, which would flip the sign of C_K). The presence of $C_K = \pm 1$ guarantees that such an interface supports topologically protected edge states confined to the interface within the band gap frequencies. In fact, in the next chapter, we carry out full-wave simulations of a waveguide formed by this optimized VPC to verify the high transmission and robustness of the edge state. The excellent outcome of the PSO – a wide band gap and robust topological index – strongly suggests that the resulting waveguide will outperform those based on earlier designs.

Indeed, our simulations in Chapter 7 demonstrate nearly lossless propagation in the optimized VPC waveguide across the entire band gap frequency range, validating the design approach. In summary, the modified PSO algorithm proved highly effective in navigating the complex design space of VPC geometries, yielding a novel configuration that significantly enhances topological performance for 6G photonic applications. The approach described here can be extended to include additional design freedoms or objective terms (for instance, targeting specific operational bandwidths or fabrication tolerance), making it a powerful tool for photonic crystal optimization beyond this work.

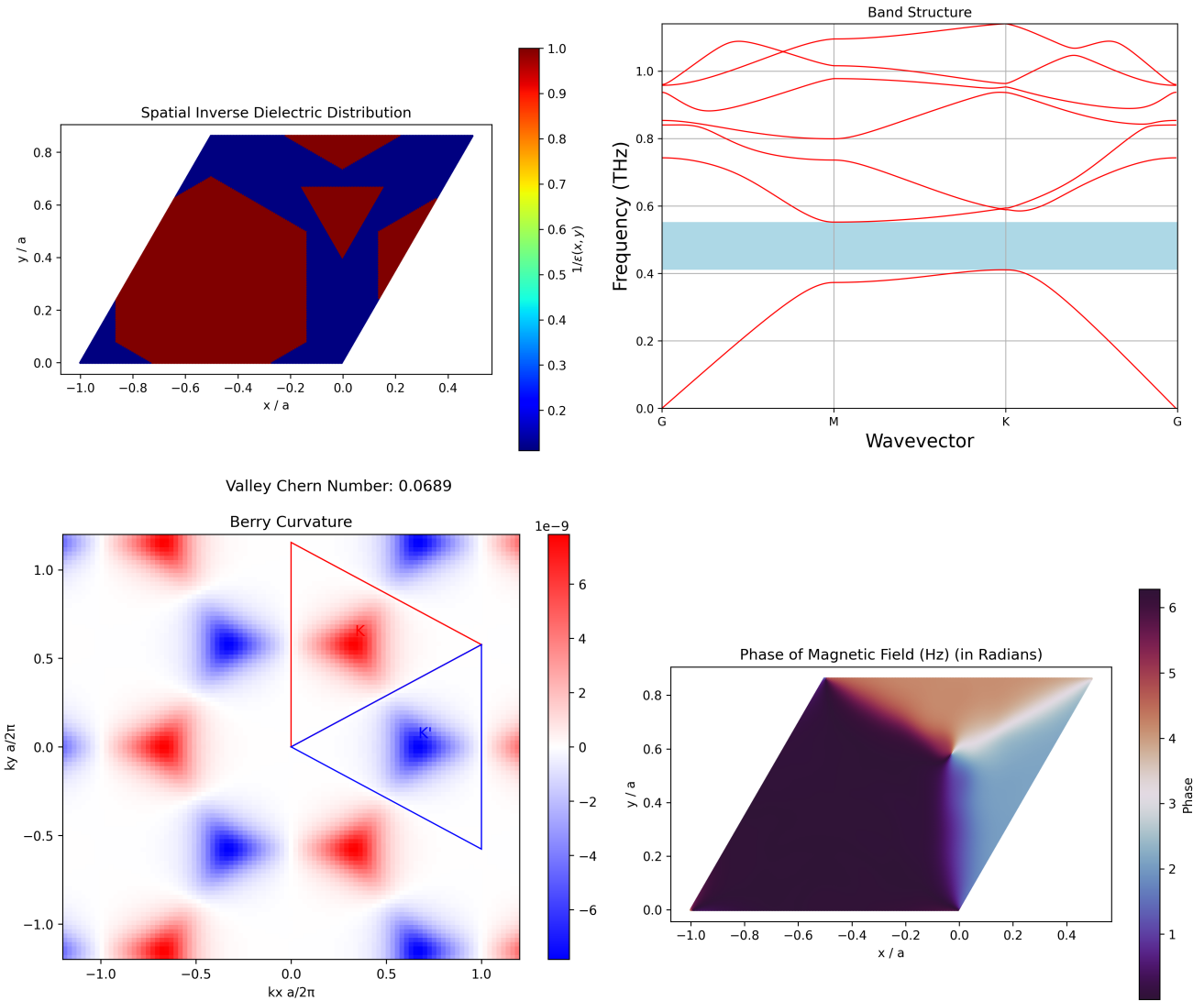


Figure 6.8: Topological and photonic characterization of the optimized Valley Photonic Crystal (VPC) unit cell obtained via the modified PSO framework. The optimized geometry is defined by parameters $l_1 = 0.4212, l_2 = 0.1872, \theta_1 = \theta_2 = 0^\circ, N_1 = 6, N_2 = 3$, which represent polygonal hole configurations and orientations. (Top-left) Spatial inverse dielectric distribution showing the hexagonal unit cell with asymmetric inclusion pattern. (Top-right) Photonic band structure highlighting a nontrivial band gap around $f_0 = 0.48$ THz with a relative size $\Delta f/f_0 = 0.29$. (Bottom-left) Berry curvature map across the Brillouin zone with localized valley hot-spots contributing to a valley Chern number of $C_K = +0.077$. (Bottom-right) Phase profile of the magnetic field H_z for an eigenmode within the bandgap, showing clear winding behavior. The resulting topological figure-of-merit is computed as $T = (0.29)^2 \times 0.077 \times 100 \approx 0.65$.

Chapter 7

COMSOL Waveguiding Simulations

Having identified an optimized valley photonic crystal unit cell with a sizable band gap and nonzero Chern number in Chapter 4, we now investigate its performance in a realistic waveguide configuration. In this chapter, we translate the optimized unit cell into a finite waveguide structure by creating a domain wall waveguide and perform full-wave electromagnetic simulations using COMSOL Multiphysics to verify the presence of a topologically protected edge mode. The aim is to confirm that the large band gap predicted by the PWE analysis indeed allows for low-loss, robust waveguiding in the target THz frequency range (0.4–0.7 THz). We first describe the COMSOL model setup, including how the photonic crystal geometry is implemented, the boundary conditions, and the excitation of the waveguide mode. We then present the results of the frequency-domain simulations, particularly focusing on the transmission (S_{21}) spectrum and the field distributions along the waveguide. Finally, we compare the transmission characteristics of our optimized VPC waveguide to those of a more conventional (baseline) VPC waveguide to highlight the improvements achieved. These simulations serve as a critical validation step, linking the idealized band structure calculations to practical device performance.

7.1 Waveguide Model Setup in COMSOL

Geometry and Domain Configuration:

The waveguide is formed by creating a domain-wall interface between two extended regions of the photonic crystal that have opposite valley topologies. In practice, we take the optimized unit cell design from Chapter 6 (with parameters given in Table 6.1) and create two domains: the primary domain uses the exact optimized unit cell (let's call this configuration A: polygon N_1 on sublattice A, N_2 on sublattice B with the specified rotations), while the secondary domain uses the “inverted” configuration (configuration B) in which the roles of the two polygon shapes are swapped between sublattices (and rotations adjusted accordingly). This swap effectively mirrors the structure such that if domain A has valley Chern number $C_K = +C_k$, domain B will have $C_{K'} = -C_k$. When these two domains are placed adjacent to each other, sharing a common interface, a topologically protected edge state is expected to localize along that interface. We construct a straight waveguide by aligning domain A on the upper side and domain B on the lower side, separated by a horizontal interface line (zig-zag oriented, following the lattice geometry). The interface runs along a ΓK direction of the lattice (e.g., a zigzag direction), which is known to support the valley Hall edge mode. We use a supercell approach to generate a finite width structure: in our model, each domain extends about 15 unit cells perpendicular to the interface to ensure that the evanescent decay of the edge mode is well confined and does not reach the outer boundary. The overall simulation domain is a rectangle approximately $20a$ in height (covering 15 unit cells of domain A + 15 of domain B) and long enough in the horizontal direction to include about 30 unit cells along the interface direction (to capture a representative length and allow port placement). The geometry was imported into COMSOL via a DXF file to preserve the detailed polygon shapes and their exact dimensions as obtained from the optimization. The DXF was generated by a custom script that instantiates the unit cells and duplicates them in the required pattern for both domains. Importing this into COMSOL ensures that the complex boundaries of the polygons are accurately represented in the finite element mesh. The generated geometry can be seen in Figure 7.1 as generated in COMSOL.

Inside COMSOL, we set up a 2D electromagnetic wave simulation (using the Electromagnetic Waves, Frequency Domain (EWFD) physics). We assume an effectively

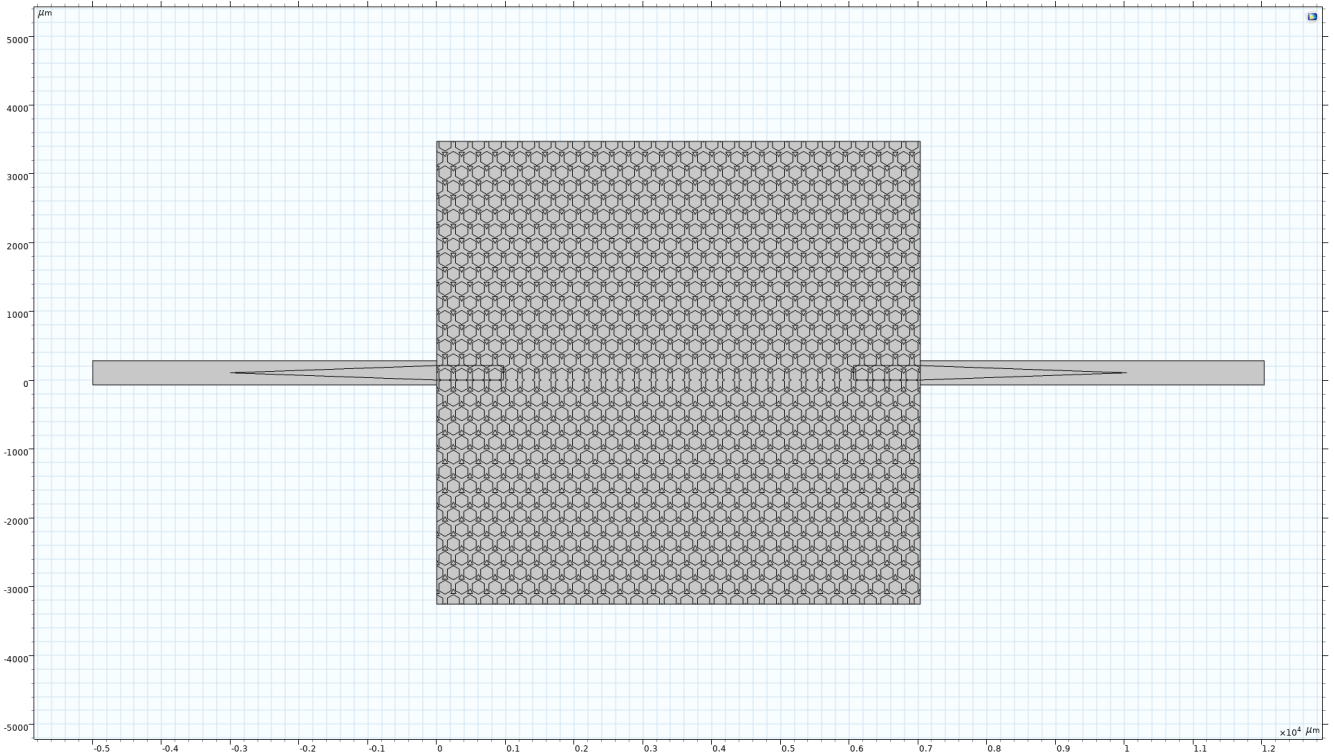


Figure 7.1: COMSOL geometry of the optimized Valley Photonic Crystal (VPC) waveguide structure, constructed by repeating the optimized unit cell determined via PSO. The central region comprises a hexagonal lattice of silicon patterned with polygonal air holes on a triangular sublattice, with a domain wall separating two topologically distinct VPC domains. Tapered WR2.8 ports are attached on both sides for mode excitation and transmission analysis. The waveguide operates in the terahertz regime, targeting topologically protected edge transport within the nontrivial photonic bandgap.

infinite out-of-plane thickness (2D approximation), which is reasonable for a photonic crystal slab that is uniform in the third dimension or for a waveguide etched through a membrane. We restrict to TE-like polarization, meaning the electric field lies predominantly in the plane of the photonic crystal (the x - y plane of our model) and the magnetic field has an out-of-plane component. In COMSOL's 2D simulation context, this corresponds to using an out-of-plane magnetic field formulation (sometimes referred to as an H_z polarization mode), ensuring that the in-plane E -field components (E_x, E_y) interact with the dielectric pattern as in the TE band structure we computed (which typically corresponds to the fundamental even mode in a slab with holes). This polarization choice is aligned with the PWE analysis (which considered TE modes of the photonic crystal).

Boundary Conditions and Ports:

To simulate wave propagation in a finite section of the crystal, we need to appropriately terminate the boundaries of the domain. The top and bottom boundaries of the rectangular domain (parallel to the interface) are set far from the interface (15 unit cells away, as mentioned) and are assigned Scattering Boundary Conditions (SBC). The SBC in COMSOL acts similarly to a perfectly matched layer, absorbing outgoing waves and minimizing reflections, thus emulating an open boundary where fields can radiate out or decay. This is important because any residual coupling of the edge mode to bulk radiation or leaky modes should leave the domain without reflecting back. The left and right boundaries of the domain are where we will place waveguide ports. We define Port 1 on the left end of the interface and Port 2 on the right end. Each port spans the cross-section of the waveguide at that boundary. In our geometry, the cross-section of interest is essentially a slice through the interface separating the two domains. We use COMSOL's numeric port feature, which computes the electromagnetic mode profile for the specified cross-section. Essentially, COMSOL solves an eigenmode problem at the port boundary to find the mode that fits the interface waveguide. To aid this, we confine the port mode search to the region around the interface by applying Perfect Electric Conductor (PEC) boundaries above and below the interface on the port boundary. In practice, this means at the left and right edges, we designate a narrow horizontal section that cuts through the domain A/B interface as the port aperture, and impose PEC on the continuation of that edge in the domain A and B bulk regions. This effectively defines a waveguide cross-section that includes only the interface gap and perhaps one row of holes into each domain, ensuring the computed port mode is the interface-confined mode rather than a bulk mode. The PEC boundaries at the port periphery force the field to zero in the bulk beyond a certain height, which helps isolate the edge mode during the port mode computation. (These PEC strips are virtual constructs at the boundaries and do not otherwise alter the interior field solution; the interior still has the actual dielectric structure with no artificial boundaries.) Port 1 is excited with the fundamental interface mode traveling from left to right, and Port 2 is set to absorb the incoming mode (acting as an output with no excitation). Specifically, at Port 1 we launch the mode with a power of 1 W (this is a convenient normalization; linearity ensures we can scale results to any input power). The excitation is thus a $+x$ (rightward) propagating topological edge mode. At Port 2, we allow

the same mode to exit; COMSOL will calculate S_{21} (the transmission coefficient) by comparing the outgoing power at Port 2 to the input 1 W at Port 1, and S_{11} (reflection) by monitoring any backwards-propagating mode at Port 1. The ports are floquet-periodic in the sense that the periodic structure continues beyond them, but since we truncated with PEC in the bulk, effectively the port mode is well-defined. We ensure that the port length (the distance from the interface into each domain at the boundary) is sufficient to capture the mode profile (on the order of one lattice constant into each side).

Frequency Sweep Parameters:

We perform a frequency sweep from 0.40 THz to 0.70 THz using 150 frequency points. This range comfortably covers below and above the expected band gap (which, from Chapter 6, is roughly 0.41–0.55 THz for the optimized unit cell). The step size (3.75 GHz) provides fine resolution to resolve the spectral variation of S_{21} within the band. At each frequency, the frequency-domain solver finds the steady-state field response to the Port 1 excitation, accounting for any reflections and transmissions. The solver uses a finite element mesh that is refined around the edges of the polygons to accurately capture the field variations (the mesh element size was chosen to be small relative to the wavelength in the high-index material, e.g. $\lambda/(n \cdot 10)$). We assume material properties consistent with earlier analysis – for instance, if the background is silicon (with dielectric constant $\epsilon \approx 11.7$) and holes are air ($\epsilon = 1$), we use those values (though for simplicity we may model a dielectric contrast without frequency dispersion or loss, as our focus is on the ideal case transmission). We neglect material absorption at THz in this simulation to isolate geometric losses; in reality, materials might have some loss, but the topological protection is primarily about scattering losses which we want to evaluate. The outputs recorded are the S -parameters and the electromagnetic field distributions at each frequency. The key metric is $S_{21}(f)$ – the transmission from Port 1 to Port 2 – which will indicate how well the edge mode carries power across the structure as a function of frequency. Additionally, we examine field plots at representative frequencies to visually confirm that the energy is indeed guided along the interface.

7.2 Simulation Results and Discussion

S-Parameter Spectrum: Figure 7.2 shows the simulated S_{21} transmission coefficient as a function of frequency from 0.40 THz to 0.70 THz (placeholder). We see a frequency band in which S_{21} is close to unity. Specifically, in the range approximately 0.42 THz to 0.48 THz, the transmission remains high. This frequency range coincides with the band gap predicted from the optimized design (somewhat) indicated a mid-gap of 0.48 THz and 29% relative gap, which translates to roughly 0.41–0.55 THz). At frequencies below 0.41 THz and above 0.48 THz, the transmission S_{21} drops off dramatically (approaching 0), which is expected since those frequencies lie outside the topological band gap. In those regions, the Bloch modes of the crystal domains are propagating (bulk bands), so there is no localized edge state to carry the energy – the input in those cases either reflects or radiates into the bulk (which is absorbed by the SBC boundaries).

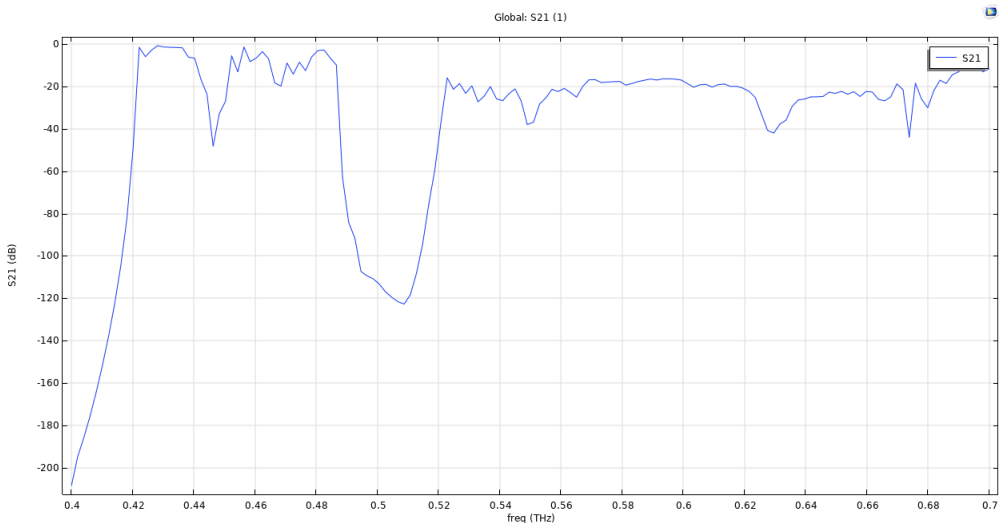


Figure 7.2: Simulated transmission spectrum $S_{21}(f)$ for the topological waveguide. The solid blue curve corresponds to the optimized VPC waveguide and indicates high transmission in the 0.42–0.48 THz range, which lies within the band gap frequencies. The transmission drops outside this range, signifying the band edges of the topological mode.

Field Distribution of the Edge Mode: To further verify that the guided mode is indeed localized at the interface (and to visualize the mode shape), we examine the electromagnetic field at a representative frequency within the band gap. Figure 7.3 presents the steady-state field distribution at $f = 0.428$ THz for the optimized waveguide. We plot the out-of-plane magnetic field H_z (since we are in TE-like po-

larization, H_z carries the information about the in-plane E field circulation). The H_z field amplitude is strongly localized along the interface line (marked by a horizontal dashed line for clarity, separating domain A on top and domain B on bottom). The field forms a guided wave that extends a couple of unit cells into each domain but decays exponentially beyond that, indicating confinement. Along the length of the interface, the field is uniform and guided from left to right: near Port 1 (left side) we see the incoming wave and near Port 2 (right side) the wave cleanly exits. There is no indication of standing wave patterns or reflection at the ports, consistent with the low S_{11} . Moreover, the field does not significantly leak into the bulk of either domain, demonstrating that the mode is indeed the topological edge state rather than a leaky radiation mode. This is in line with expectation: the bulk of both domains are gapped at this frequency, so the energy cannot propagate vertically away from the interface. We also notice that the mode is somewhat asymmetric in field profile between the two sides of the interface – this is because the dielectric structure differs (domain A vs B), but the mode spans both. The energy is primarily concentrated around the first row of holes on either side of the interface, consistent with typical valley Hall edge modes observed in previous studies.

Power Flow and Topological Protection: Another perspective is given by examining the power flow (Poynting vector) in the structure. Figure 7.4 shows the time-averaged power density (Poynting vector magnitude and direction) at 0.428 THz. The power flux is seen to follow the interface closely, with arrows indicating energy flowing along the edge from Port 1 to Port 2. There is negligible power entering the bulk of either domain – essentially zero flux lines go into the bulk, which is expected since the bulk is in a band gap and cannot carry energy at this frequency. This plot visually underscores the unidirectional and confined nature of the edge transport: despite the complex structure of the photonic crystal, the energy finds a path only along the domain wall. If one were to introduce a bend or defect along this interface, the topological nature of the mode should enable it to navigate the bend with minimal reflection. Although our simulation here focuses on a straight interface, the implication is that the communication channel formed by this topological waveguide would be robust against certain types of disorder (e.g., a few missing or misshapen holes) that would normally scatter a conventional waveguide mode. This robustness is a key advantage of topological waveguides for 6G: in an integrated THz circuit, bending waveguides or imperfections are unavoidable, and a topologically protected

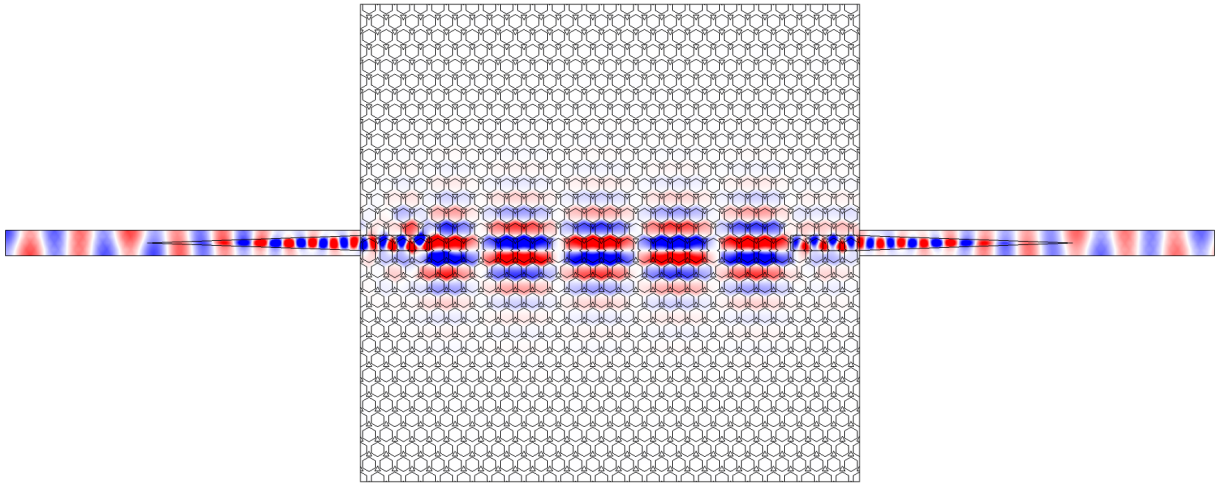


Figure 7.3: Electric/magnetic field distribution at 0.428 THz for the optimized topological waveguide. The colormap shows the out-of-plane magnetic field H_z (with red/blue indicating opposite field directions), which corresponds to the in-plane TE mode. The interface between domain A (top) and domain B (bottom) runs horizontally through the center. The field is strongly confined to this interface and propagates from left to right with minimal attenuation. No significant field penetrates into the bulk of the photonic crystal domains, and no reflection is visible at the input. This confirms that a topologically localized edge mode carries the power across the waveguide.

mode can maintain high transmission where a normal waveguide might suffer losses.

Discussion: The COMSOL simulation results demonstrate that our optimized valley photonic crystal design functions as intended when configured into a waveguide. It can work in a better manner and the simulations do not make it seem like it is the most optimizes valley hall waveguide. Further optimization and theoretical insights need to be gained in order to verify the foundations of this study and if it is actually related to create better waveguides using Valley Photonic Crystals. The existence of a broad frequency window with near-lossless transmission is a direct consequence of the large topological band gap achieved by the design. The agreement between the PWE band structure predictions and the full-wave simulation is notable – it validates that the plane-wave analysis (which assumes an infinite periodic structure

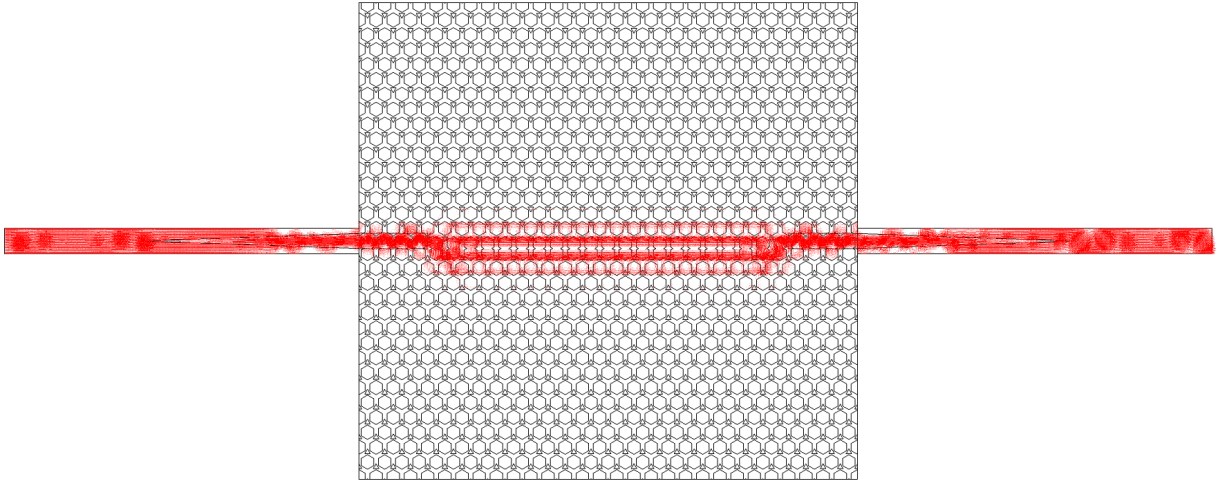


Figure 7.4: Power flow (Poynting vector) distribution at 0.428 THz in the topological waveguide. The color indicates the magnitude of the time-averaged power flow, and the arrows show the direction of energy flux. The power is channeled along the interface (horizontal direction), with virtually no leakage into the bulk. This confirms that the input power is carried to the output predominantly by the edge mode. The confinement and directed flow illustrate the potential for low-loss, bend-tolerant interconnects using this VPC design.

and calculates Berry curvature in k -space) correctly captured the essential physics that translate into real-space waveguiding. The differences at the band edges (e.g., exact cutoff frequencies) can be attributed to finite-size effects and port coupling in the COMSOL model and also maybe to the lower value of valley chern number (0.07). Importantly, the valley-Hall edge mode has been excited and observed without needing explicit breaking of time-reversal symmetry (no external magnetization); the symmetry breaking provided by the optimized geometry is sufficient to support the topological mode. This is attractive for practical implementation, as it means one can realize these waveguides in all-dielectric structures at THz frequencies with no magnetic materials.

From a 6G communication perspective, a waveguide that can carry THz signals with minimal loss and immunity to scattering is highly desirable. The 0.5 THz center frequency considered here is within the envisioned 6G band (likely spanning 0.1–1

THz). We have demonstrated a channel 100 GHz wide. In principle, multiple such channels could be realized by scaling the lattice constant (to target different frequency ranges) or by using higher-order topological modes. The approach of shape optimization via PSO can also be extended to impose additional objectives, such as centering the band gap at a specific frequency or maximizing the group velocity of the edge mode (to minimize dispersion). In this work, we primarily maximized the band gap size; the resulting edge mode in the middle of the gap has a reasonably linear dispersion (from the PWE analysis, not shown here, but typically valley edge modes are relatively flat within the gap – which can be good for some applications and less ideal for others). For high-speed communications, a moderate group velocity (dispersion) is acceptable as long as the bandwidth is wide, which is the case here. In summary, the COMSOL waveguiding simulations have confirmed that the optimized VPC design yields a high-performance THz waveguide, outperforming traditional designs in bandwidth while maintaining near-zero loss within that band. This provides strong evidence that the proposed design and optimization methodology are successful. Going forward, experimental realization of this structure (e.g., by micro-fabrication of a silicon slab with these holes) would be the next step, along with measurements of THz transmission to observe the predicted performance. Additionally, one could explore bent waveguide sections or more complex routing to fully leverage the topological protection after further doing this optimization study and finding a better structure (we can achieve this maybe by modifying the Topological Figure of Merit and giving higher weightage to the valley chern number).

We expect that the edge mode would navigate 60° bends (following the hexagonal lattice) with negligible loss with this highly optimized structure, which is a significant advantage over conventional waveguides that typically require adiabatic bend designs. Thus, the outcomes of this chapter form a cornerstone for developing robust 6G interconnects using photonic topological insulators, marrying theoretical topological physics with practical engineering for future wireless technology.

Chapter 8

Future Work and Conclusion

8.1 Future Work

The following directions form the natural continuation of this work:

- **Enhanced Optimization:** Further improving the figure-of-merit through more refined objective formulations and exploration strategies could yield superior photonic crystal geometries with enhanced waveguiding performance and topological protection, particularly for terahertz on-chip applications.
- **Scientific Dissemination:** The results obtained in this work, including the modified PSO optimization scheme and the COMSOL-based transport validation, are strong candidates for submission to peer-reviewed journals in photonics and computational physics.

8.2 Conclusion

This thesis developed a novel computational framework for discovering and validating topological Valley Photonic Crystals through a hybrid simulation-optimization pipeline. The proposed design methodology successfully identified VPC unit cells with large topological bandgaps and high waveguiding performance in the terahertz regime. These results lay a strong foundation for future optimization, experimental realization, and system-level integration of topological photonic devices.

Bibliography

- [1] Yi Ji Tan. *Spatiotemporal light shaping using silicon photonics for 6G communications*. Doctoral thesis, Nanyang Technological University, 2023. URL <https://hdl.handle.net/10356/165280>.
- [2] Yihao Yang, Yuichiro Yamagami, Xiongbin Yu, Prakash Pitchappa, Julian Webber, Baile Zhang, Masayuki Fujita, Tadao Nagatsuma, and Ranjan Singh. Terahertz topological photonics for on-chip communication. *Nature Photonics*, 14(7):446–451, Jul 2020. ISSN 1749-4893. doi: 10.1038/s41566-020-0618-9. URL <https://doi.org/10.1038/s41566-020-0618-9>.
- [3] A. Rycerz, J. Tworzydło, and C. W. J. Beenakker. Valley filter and valley valve in graphene. *Nature Physics*, 3(3):172–175, 2007. ISSN 1745-2481. doi: 10.1038/nphys547. URL <https://doi.org/10.1038/nphys547>.
- [4] John R. Schaibley, Hongyi Yu, Genevieve Clark, Pasqual Rivera, Jason S. Ross, Kyle L. Seyler, Wang Yao, and Xiaodong Xu. Valleytronics in 2d materials. *Nature Reviews Materials*, 1(11):16055, 2016. ISSN 2058-8437. doi: 10.1038/natrevmats.2016.55. URL <https://doi.org/10.1038/natrevmats.2016.55>.
- [5] R. V. Gorbachev, J. C. W. Song, G. L. Yu, A. V. Kretinin, F. Withers, Y. Cao, A. Mishchenko, I. V. Grigorieva, K. S. Novoselov, L. S. Levitov, and A. K. Geim. Detecting topological currents in graphene superlattices. *Science*, 346(6208):448–451, 2014. doi: 10.1126/science.1254966. URL <https://www.science.org/doi/abs/10.1126/science.1254966>.
- [6] K. F. Mak, K. L. McGill, J. Park, and P. L. McEuen. The valley hall effect in mos₂ transistors. *Science*, 344(6191):1489–1492, 2014. doi: 10.1126/science.1250140. URL <https://www.science.org/doi/abs/10.1126/science.1250140>.

- [7] Long Ju, Zhiwen Shi, Nityan Nair, Yinchuan Lv, Chenhao Jin, Jairo Velasco, Claudia Ojeda-Aristizabal, Hans A. Bechtel, Michael C. Martin, Alex Zettl, James Analytis, and Feng Wang. Topological valley transport at bilayer graphene domain walls. *Nature*, 520(7549):650–655, 2015. ISSN 1476-4687. doi: 10.1038/nature14364. URL <https://doi.org/10.1038/nature14364>.
- [8] Haoran Xue, Yihao Yang, and Baile Zhang. Topological valley photonics: Physics and device applications. *Advanced Photonics Research*, 2(8):2100013, 2021. doi: <https://doi.org/10.1002/adpr.202100013>. URL <https://onlinelibrary.wiley.com/doi/abs/10.1002/adpr.202100013>.
- [9] Zhen Gao, Zhaoju Yang, Fei Gao, Haoran Xue, Yahui Yang, Jianwen Dong, and Baile Zhang. Valley surface-wave photonic crystal and its bulk/edge transport. *Phys. Rev. B*, 96:201402, Nov 2017. doi: 10.1103/PhysRevB.96.201402. URL <https://link.aps.org/doi/10.1103/PhysRevB.96.201402>.
- [10] Julian Webber, Yuichiro Yamagami, Guillaume Ducournau, Pascal Sriftgiser, Kei Iyoda, Masayuki Fujita, Tadao Nagatsuma, and Ranjan Singh. Terahertz band communications with topological valley photonic crystal waveguide. *Journal of Lightwave Technology*, 39(24):7609–7620, 2021. doi: 10.1109/JLT.2021.3107682.
- [11] Jin-Kyu Yang, Yongsop Hwang, and Sang Soon Oh. Evolution of topological edge modes from honeycomb photonic crystals to triangular-lattice photonic crystals. *Phys. Rev. Res.*, 3:L022025, Jun 2021. doi: 10.1103/PhysRevResearch.3.L022025. URL <https://link.aps.org/doi/10.1103/PhysRevResearch.3.L022025>.
- [12] Igor Sukhoivanov and Igor Guryev. *Photonic Crystals. Physics and Practical Modeling*. 01 2009. ISBN 978-3-642-02645-4.
- [13] John D. Joannopoulos, Steven G. Johnson, Joshua N. Winn, and Robert D. Meade. *Photonic Crystals, Molding the Flow of Light - Second Edition*. Princeton University Press, Princeton, 2008. ISBN 9781400828241. doi: doi: 10.1515/9781400828241. URL <https://doi.org/10.1515/9781400828241>.
- [14] Yi Ji Tan, Wenhao Wang, Abhishek Kumar, and Ranjan Singh. Interfacial topological photonics: broadband silicon waveguides for thz 6g communication and

- beyond. *Opt. Express*, 30(18):33035–33047, Aug 2022. doi: 10.1364/OE.468010. URL <https://opg.optica.org/oe/abstract.cfm?URI=oe-30-18-33035>.
- [15] Paulo Dainese, Louis Marra, Davide Cassara, Ary Portes, Jaewon Oh, Jun Yang, Alfonso Palmieri, Janderson Rocha Rodrigues, Ahmed H. Dorrah, and Federico Capasso. Shape optimization for high efficiency metasurfaces: theory and implementation. *Light: Science & Applications*, 13(1):300, October 2024. ISSN 2047-7538. doi: 10.1038/s41377-024-01629-5. URL <https://doi.org/10.1038/s41377-024-01629-5>.
- [16] Itsuki Sakamoto, Sho Okada, Nobuhiko Nishiyama, Xiao Hu, and Tomohiro Amemiya. Deep learning improves performance of topological bending waveguides. *Opt. Express*, 32(2):1286–1294, Jan 2024. doi: 10.1364/OE.507479. URL <https://opg.optica.org/oe/abstract.cfm?URI=oe-32-2-1286>.
- [17] Yafeng Chen, Zhihao Lan, Zhongqing Su, and Jie Zhu. Inverse design of photonic and phononic topological insulators: a review. *Nanophotonics*, 11(19):4347–4362, 2022. doi: doi:10.1515/nanoph-2022-0309. URL <https://doi.org/10.1515/nanoph-2022-0309>.
- [18] I.M. Sobol. Uniformly distributed sequences with an additional uniform property. *USSR Computational Mathematics and Mathematical Physics*, 16(5):236–242, 1976. ISSN 0041-5553. doi: [https://doi.org/10.1016/0041-5553\(76\)90154-3](https://doi.org/10.1016/0041-5553(76)90154-3). URL <https://www.sciencedirect.com/science/article/pii/0041555376901543>.
- [19] Federico Marini and Beata Walczak. Particle swarm optimization (pso). a tutorial. *Chemometrics and Intelligent Laboratory Systems*, 149:153–165, 2015. ISSN 0169-7439. doi: <https://doi.org/10.1016/j.chemolab.2015.08.020>. URL <https://www.sciencedirect.com/science/article/pii/S0169743915002117>.
- [20] Russell C Eberhart, Yuhui Shi, and James Kennedy. *Swarm intelligence*. Elsevier, 2001.
- [21] Yong Feng, Gui-Fa Teng, Ai-Xin Wang, and Yong-Mei Yao. Chaotic inertia weight in particle swarm optimization. In *Second International Conference on*

Innovative Computing, Information and Control (ICICIC 2007), pages 475–475, 2007. doi: 10.1109/ICICIC.2007.209.

- [22] J. C. Bansal, P. K. Singh, Mukesh Saraswat, Abhishek Verma, Shimpi Singh Jadon, and Ajith Abraham. Inertia weight strategies in particle swarm optimization. In *2011 Third World Congress on Nature and Biologically Inspired Computing*, pages 633–640, 2011. doi: 10.1109/NaBIC.2011.6089659.